Ocean Engineering 121 (2016) 239–253

Contents lists available at ScienceDirect

Ocean Engineering

journal homepage: www.elsevier.com/locate/oceaneng

Theoretical and numerical estimation of ship-to-ship hydrodynamic interaction effects

Zhi-Ming Yuan [a], Chun-Yan Ji [b,*], Atilla Incecik [a], Wenhua Zhao [c], Alexander Day [a]

[a] Department of Naval Architecture, Ocean and Marine Engineering, University of Strathclyde, Glasgow, UK
[b] School of Naval Architecture and Ocean Engineering, Jiangsu University of Science and Technology, Zhenjiang, China
[c] Centre for Offshore Foundation Systems (M053), The University of Western Australia, 35 Stirling Highway, Crawley, WA 6009, Australia

ARTICLE INFO

Article history:
Received 8 May 2015
Received in revised form
9 May 2016
Accepted 17 May 2016

Keywords:
Hydrodynamic interaction
Rankine source method
Far-field wave pattern
Boundary element method
Ship-to-ship problem
Forward speed effects

ABSTRACT

The main objective of this paper is to investigate theoretically and numerically how much interactions are expected between two ships travelling in waves. The theoretical estimation is based on asymptotic far-field wave patterns produced by a translating and oscillating source. The far-field wave pattern is governed by the parameter $\tau=\omega_e u_0/g$; For values of the parameter $\tau>0.25$ there exist a fan-shaped quiescent region in front of the vessel. As τ increases, the range of the fan-shaped quiescent region will be expanded. The critical line between the quiescent and wake region can be estimated by the asymptotic expressions theoretically. It is expected that there is no hydrodynamic interaction if the two ships are located in each other's fan-shaped quiescent region. But due to the near-field local waves produced by the 3-D ships, the critical line could be different from that estimated from asymptotic wave pattern. Therefore, we developed a 3-D panel method based on Rankine-type Green function to investigate the hydrodynamic interaction effects for several combinations of parameters, including oscillation frequency, forward speed and transverse distance between two ships. Finally, the critical line calculated numerically was presented and compared to the theoretical estimation.

1. Introduction

Interest in the prediction of the hydrodynamic interactions between two advancing ships has grown in recent years as the ships have to pass each other in close proximity in harbour areas and waterways with dense shipping traffic. The behaviour of two ships in waves with speed effect is of special concern to the Navy, that is, for underway replenishment, and for other commercial purposes.

Fang and Kim (1986) firstly took forward speed into consideration in ship-to-ship problem. They utilized a 2-D procedure, including the hydrodynamic interaction and an integral equation method, to predict the coupled motions between two ships advancing in oblique seas. They found that the roll motion was reduced while the ships were advancing. However, due to the 2-D assumptions, some deficiencies including the special treatment of the convective term still exist. Chen and Fang (2001) extended Fang's method (Fang and Kim, 1986) to 3-D. They used a 3-D Green function method to investigate the hydrodynamic problems between two moving ships in waves. It was found that the hydrodynamic interactions calculated by 3-D method were more reasonable in the resonance region, where the responses were not as significant as predicted by 2-D method. However, their method was only validated by model tests with zero speed. More rigorous validation should be carried out by further experiments. McTaggart et al. (2003) and Li (2007) used the model test data from Li (2001) to verify their numerical programmes, which was based on 3-D Green function method. The numerical predictions and experiments showed that the presence of a larger ship could significantly influence the motions of a smaller ship in close proximity. But the numerical prediction of roll motion was not accurate. Xu and Faltinsen (2011) used the model test data from Ronæss (2002) to verify their numerical programme based on 3-D Rankine source method. They applied an artificial numerical beach to satisfy the radiation condition. They found that the hydrodynamic peaks and spikes were related to the resonance modes in the gap between the hulls. However, they also failed to predict the roll motion precisely. Within the frame work of Green function, Xu and Dong (2013) developed a 3-D translating-pulsating (3DTP) source method to calculate wave loads and free motions of two ships advancing in waves. Model tests were carried out to measure the wave loads and the free motions for a pair of side-by-side arranged ship models advancing with an identical speed in head regular waves. Both the experimental and the numerical predictions

* Corresponding author.
E-mail address: jichunyanjkd@163.com (C.-Y. Ji).

http://dx.doi.org/10.1016/j.oceaneng.2016.05.032

showed that hydrodynamic interaction effects on wave loads and free motions were significant. Most recently, Yuan et al. (2015a, 2014a, 2015b) developed a 3-D Rankine source panel method to investigate the hydrodynamic interactions between two ships travelling in shallow water. They used a new modified Sommerfeld radiation condition which was applicable to a wide range of forward speeds, including very low forward speed problem where the parameter τ ($\tau=\omega_e u_0/g$, ω_e is the encounter frequency, u_0 is the forward speed, and g is the gravity acceleration) is smaller than 0.25. Their method was validated through model experiments and a very large sway force was predicted when the transverse distance between two ships equalled to the wavelength. They also found that the hydrodynamic interactions between two ships were caused by the scattered waves.

The hydrodynamic interaction between two advancing ships is very important. Because of the hydrodynamic interactions, even relatively small wave can induce large motions of the smaller ship due to the nearness of the larger ship. In order to minimize the hydrodynamic interactions, we attempt to establish a rapid approach to find the relationship between the minimum spacing and the parameter τ. The minimum spacing here is referred as the minimum transverse distance between two ships that the hydrodynamic interaction is not expected. The optimum hull spacing of a family of multihulls was firstly investigated by Tuck and Lazauskas (1998). They used a thin-ship theory to optimize the multihull configurations for minimum wave-making. The optimum configurations were determined for two, three and four-hulled vessels, with and without longitudinal stagger. The generated wave amplitude, wave resistance and total drag were calculated and compared in their study. Battistin (2000) and Yang et al. (2002) also carried out hydrodynamic optimization for a trimaran. However, these studies mainly considered the calm-water case, in order to minimise wave making. Day and Doctors (2001) developed a rapid method to estimate the near- and far-field wave wake. They applied this method to the optimization of a monohull and a catamaran. But the multihulls were treated as a rigid body with 6 degrees of freedom (DoF). No attempt was made to optimise the hydrodynamic interactions between two ships (12 DoF) advancing in waves, since the motions of the ships could make the problem more complex. The main aim of the study presented in this paper is to establish a rapid method to evaluate the hydrodynamic interaction between two ships advancing in waves, in order to provide an optimum configuration of two ships. No attempt is made here to optimise the shape of individual hulls.

2. Theoretical estimation of the critical line

2.1. Background

For a single marine vessel advancing in calm-water, the so-called Kelvin wake can be observed. It is set up by a ship in steady motion and to be confined within a wedge of semi-angle $\sin^{-1}(1/3)$ in deep water. Lighthill (1978) used the stationary phase method to investigate this Kelvin angle. It can be observed from the Kelvin wake that the free surface can be divided into two regions by a critical line: wake region confined within the Kelvin angle and quiescent region outside the Kelvin angle. For the ships travelling in waves, except the Kelvin wave system, there exist two ($\tau>0.25$) or three ($\tau<0.25$) unsteady wave systems due to the oscillation of the ship (Becker, 1958; Wehausen, 1960).

Similar to the steady wave problem, the free surface of an oscillating and translating body can also be divided into two regions: wake region confined within a semi-wedge angle θ and quiescent region outside θ. However, for the unsteady ship motion, the range of the wedge is not a constant value. It varies with the parameter τ

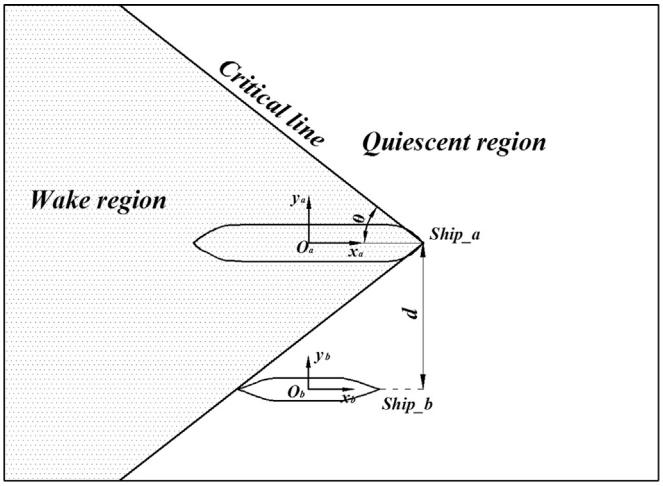

Fig. 1. Sketch of ship-to-ship with forward speed problem.

(Lighthill, 1967; Noblesse, 2001; Noblesse and Hendrix, 1992). For the parameter $\tau>0.25$, there exists a fan-shape quiescent region in front of the vessel. As τ increases, the range of the fan-shape quiescent region will be expanded. Kashiwagi and Ohkusu (1989, 1991) used the asymptotic wave contour to estimate the side-wall effect. They also extended Newman (1978) unified slender-ship theory and developed a new method to calculate the side-wall effect numerically. The critical line obtained numerically was presented and compared to the results estimated from asymptotic wave contour. Faltinsen (2006) derived a wave angle to investigate the wave interference between the waves generated by each hull of a multihull vessel. However, this wave angle was not validated from numerical calculation. In order to investigate how much the hydrodynamic interaction would be minimised if Ship_b is located in the quiescent region of Ship_a (as shown in Fig. 1), a massive numerical calculations are required to analyse several combinations of parameters, including oscillation frequency, forward speed and transverse distance between two ships. This is the main objective of the present study. Before the numerical calculation, a theoretical estimation should be established based on the asymptotic wave contour. In the present paper, we will use the Havelock form of Green function to investigate the far-field wave patterns generated by a translating and oscillating source in infinite water depth and then establish a rapid estimation of the critical line between the quiescent and wake region.

2.2. Far-field wave patterns

In order to obtain the critical line between the quiescent and wake region, the formulations of far-field asymptotic wave patterns should be established. The far-field unsteady wave pattern had been made more than half a century ago by Hanaoka (1953) and Eggers (1957). Becker (1958) also investigated the far-field wave pattern produced by a harmonic pulsating source. He provided a curves of equal phase for the various systems of waves formed. The 3-D frequency-domain analysis of the flow about a ship advancing in waves was pioneered by Chang (1977). Similar numerical work can be found by Inglis and Price (1982), Wu and Eatock Taylor (1987, 1989), Rahman (1990), Iwashita (1997). Noblesse and Hendrix (1992) derived the far-field wave patterns of a ship advancing in waves by using a stationary phase method. They derived the so-called cusp angle for different wave systems. The far-field behaviour of a 3-D pulsating source of Michell type with forward speed was also studied by Miao et al. (1995) by using the Fourier transformation and contour integration technique. More recent research on far-field wave patterns and their characteristics

were presented by Xu et al. (2013) by using a Havelock form Green function method.

According to Iwashita (1997) and Xu et al. (2013), the Havelock form of Green function is given in the following form

$$G = \frac{1}{4\pi}\left(\frac{1}{r} - \frac{1}{r'}\right) + \frac{\mathrm{i}}{2\pi}k_0 T(X, Y, Z) \tag{1}$$

where

$$\left.\begin{matrix} r \\ r' \end{matrix}\right\} = \sqrt{(x-x')^2 + (y-y')^2 + (z \mp z')^2} \tag{2}$$

$$\begin{bmatrix} 1 \\ \nabla \end{bmatrix} T(X, Y, Z) = -\frac{\mathrm{i}}{2\pi}\int_0^{\pi}\sum_{i,j=1}^{2}(-1)^{i-1}\frac{\begin{bmatrix} 1 \\ k_0\nabla \end{bmatrix} I_{ij}(k_i\varpi_j)}{\sqrt{1-4\tau\ \cos\ \theta}}d\theta \tag{3}$$

$$\left.\begin{aligned} I_{ij}(k_i\varpi_j) &= k_i F_0(k_i\varpi_j) \\ \nabla I_{ij}(k_i\varpi_j) &= \begin{bmatrix} \mathrm{i}\ \cos\ \theta \\ (-1)^{j-1}\mathrm{i}\ \sin\ \theta \\ 1 \end{bmatrix} k_i^2\left[F_0(k_i\varpi_j) - \frac{1}{k_i\varpi_j}\right] \\ F_0(k_i\varpi_j) &\equiv e^{k_i\varpi_j}\left[E_1(k_i\varpi_j) + 2\pi\mathrm{i}H_{ij}\right] \\ k_i &= \frac{1}{2\cos^2\theta}\left[1 - 2\tau\ \cos\ \theta + (-1)^i\sqrt{1-4\tau\ \cos\ \theta}\right] \end{aligned}\right\} \quad (i=1,2;\ j=1,2), \tag{4}$$

$$\varpi_j = Z + \mathrm{i}\left[X\ \cos\ \theta + (-1)^{j-1}Y\ \sin\ \theta\right], \quad Z = k_0(z'+z),$$
$$X = k_0(x-x'), \quad Y = k_0|y'-y|$$

$$E_1(k_i\varpi_j) = \int_{k_i\varpi_j}^{\infty}\frac{e^{-t}}{t}dt, \quad k_0 = \frac{g}{u_0^2}$$

The control factors are defined as

$$H_{1j} = \begin{cases} -1 & \mathrm{Re}(k_1\varpi_j) \le 0,\ \mathrm{Im}(k_1\varpi_j) < 0 \\ 0 & \mathrm{Im}(k_1\varpi_j) < 0 \end{cases},$$

$$H_{1j} = \begin{cases} 1 & \mathrm{Re}(k_2\varpi_j) \le 0,\ \mathrm{Im}(k_2\varpi_j) > 0 \\ 0 & \mathrm{Im}(k_2\varpi_j) \le 0 \end{cases}, \quad \theta \in [0, \nu];$$

$$H_{1j} = \begin{cases} 1 & \mathrm{Im}(k_1\varpi_j) < 0 \\ 0 & \mathrm{Im}(k_1\varpi_j) < 0 \end{cases}, \quad H_{2j} = \begin{cases} -1 & \mathrm{Im}(k_2\varpi_j) \le 0 \\ 0 & \mathrm{Im}(k_2\varpi_j) > 0 \end{cases} \quad \theta \in \left[\nu, \frac{\pi}{2}\right];$$

$$H_{1j} = \begin{cases} 1 & \mathrm{Im}(k_1\varpi_j) \ge 0 \\ 0 & \mathrm{Im}(k_1\varpi_j) < 0 \end{cases}, \quad H_{2j} = \begin{cases} 1 & \mathrm{Im}(k_2\varpi_j) \ge 0 \\ 0 & \mathrm{Im}(k_2\varpi_j) < 0 \end{cases} \quad \theta \in \left[\frac{\pi}{2}, \pi\right]$$

(x, y, z) and (x', y', z') denotes the position vector of the field point and source point respectively. Then the free-surface elevation can be expressed as

$$\begin{aligned} \zeta(x, y, x', y', z', t) &= \mathrm{Re}\left[\Xi(x, y, x', y', z')e^{-\mathrm{i}\omega_e t}\right]_{z=0} \\ &= \mathrm{Re}\left[\frac{1}{g}\left(\mathrm{i}\omega_e G + u_0\frac{\partial G}{\partial x}\right)e^{-\mathrm{i}\omega_e t}\right]_{z=0} \end{aligned} \tag{5}$$

where Ξ is the spatial expression of the free-surface elevation. By substituting Eqs. (1)–(4) into Eq. (5), the time independent wave shape function can be written as

$$\begin{aligned} \zeta(x, y, x', y', z') = &\sum_{j=1}^{2}\int_0^{\nu}F_{1j}(\theta)d\theta + \sum_{j=1}^{2}\int_0^{\nu}F_{2j}(\theta)d\theta + \sum_{j=1}^{2}\int_{\nu}^{\pi}F_{1j}(\theta)d\theta \\ &+ \sum_{j=1}^{2}\int_{\nu}^{\pi/2}F_{2j}(\theta)d\theta + \sum_{j=1}^{2}\int_{\pi/2}^{\pi}F_{2j}(\theta)d\theta \end{aligned} \tag{6}$$

where

$$F_{ij}(\theta) = (-1)^{i-1}\frac{\mathrm{i}k_0k_i\left[\omega_e F_0(k_j\varpi) + u_0k_0\ \cos\ \theta(F_0(k_j\varpi)k_i - \varpi_j^{-1})\right]}{4\pi^2 g\sqrt{1-4\tau\ \cos\ \theta}} \tag{7}$$

$$\nu = \begin{cases} 0, & (\tau < 0.25) \\ \cos^{-1}\left(\frac{1}{4\tau}\right), & (\tau > 0.25) \end{cases} \tag{8}$$

In the far-field, as $X^2+Y^2\to\infty$, $e^{k_j\varpi}E_1(k_j\varpi)$ and $\frac{1}{\varpi}$ in Eq. (4) tend to be zero (Takagi, 1992), and Eq. (7) can be reduced to

$$F_{ij}(\theta) = (-1)^i\frac{k_0k_iH_{ij}(\omega_e + u_0k_0k_i\ \cos\ \theta)}{2\pi g\sqrt{1-4\tau\ \cos\ \theta}}e^{k_iZ+\mathrm{i}\psi_{ij}} \tag{9}$$

The phase function ψ can be defined as

$$\psi_{ij} = k_i\left[X\ \cos\ \theta + (-1)^{j-1}Y\ \sin\ \theta\right] \tag{10}$$

By denoting $\kappa_i = -k_i\ \cos\ \theta$ when $\omega_e \ne 0$ and $u \ne 0$ (the discussion on the case of $\omega_e = 0$ and $u = 0$ can be found in Xu et al. (2013)), Eq. (9) can be written as

$$F_{ij}(\kappa_i) = \frac{k_0(\kappa_i-\tau)^3H_{ij}(\omega_e - uk_0\kappa_i)}{2\pi g(\kappa_i+\tau)}e^{(\kappa_i-\tau)^2Z+\mathrm{i}\psi_{ij}} \tag{11}$$

where

$$\psi_{ij} = -X\kappa_i + (-1)^{j-1}Y\sqrt{(\kappa_i-\tau)^4 - \kappa_i^2} \tag{12}$$

It is well known within the frame work of stationary phase method that the main contribution to the wave term comes from the points where $d\psi_{ij}/d\kappa_i = 0$ in the far-field as $X^2+Y^2\to\infty$. Thus, we can obtain the following expression:

$$X = (-1)^{j-1}\frac{Y\left[2(\kappa_i-\tau)^3 - \kappa_i\right]}{\sqrt{(\kappa_i-\tau)^4 - \kappa_i^2}} \tag{13}$$

Let the source point locate at $(x', y', z')=(0, 0, z')$, $z<0$. By substituting Eq. (13) into Eq. (12), the parametric equations can be expressed as

$$\left.\begin{aligned} k_0x &= \psi_{ij}\frac{2(\kappa_i-\tau)^3 - \kappa_i}{(\kappa_i-\tau)^3(\kappa_i+\tau)} \\ k_0|y| &= (-1)^j\psi_{ij}\frac{\sqrt{(\kappa_i-\tau)^4 - \kappa_i^2}}{(\kappa_i-\tau)^3(\kappa_i+\tau)} \end{aligned}\right\} \tag{14}$$

The constant-phase curves defined by Eq. (14) are depicted in Fig. 2 for a set of values of ψ_{ij} with increment equal to 2π. It can be found in Fig. 2(a) that at $\tau<0.25$, there are three distinct wave systems: one ring wave system, which are approximately elliptical in shape, and two Kelvin fan wave systems confined within two distinct wedges, which can be referred as "outer and inner V waves". The ring waves are dense in the positive x-axis and sparse in the negative x-axis. At $\tau>0.25$, as shown in Fig. 2(b), the upstream portion of the ring waves do not exist. The wave-pattern plots for values of $\tau\to0.25^+$and $\tau\to0.25^-$ can be found in Noblesse and Hendrix (1992). It should also be noted from Eq. (14) that only concentric circle ring waves will exist when $u_0=0$, which presents the feature as a 3-D pulsating source without forward speed. Another interesting finding at the case of $u_0\ne0$ and $\omega_e=0$ is that the ring waves vanish and the inner and outer V waves merge together as Kelvin waves. Furthermore, as $\kappa_i\to-\tau$, $x^2+y^2\to\infty$, and the intervals $-\infty<\kappa_i<-\tau$ and $-\tau<\kappa_i<\nu_5$ (the value of ν_5 will be discussed further on) corresponds to two branches of the fan waves, which can be called inner and outer fan waves respectively, as shown in Fig. 3.

2.3. Semi-wedge angle and the minimum spacing

The critical line shown in Fig. 1 can be determined by the semi-angle θ, which may be referred as semi-wedge angle hereafter. From Fig. 2(a) we can find that at $\tau<0.25$, this semi-angle θ does

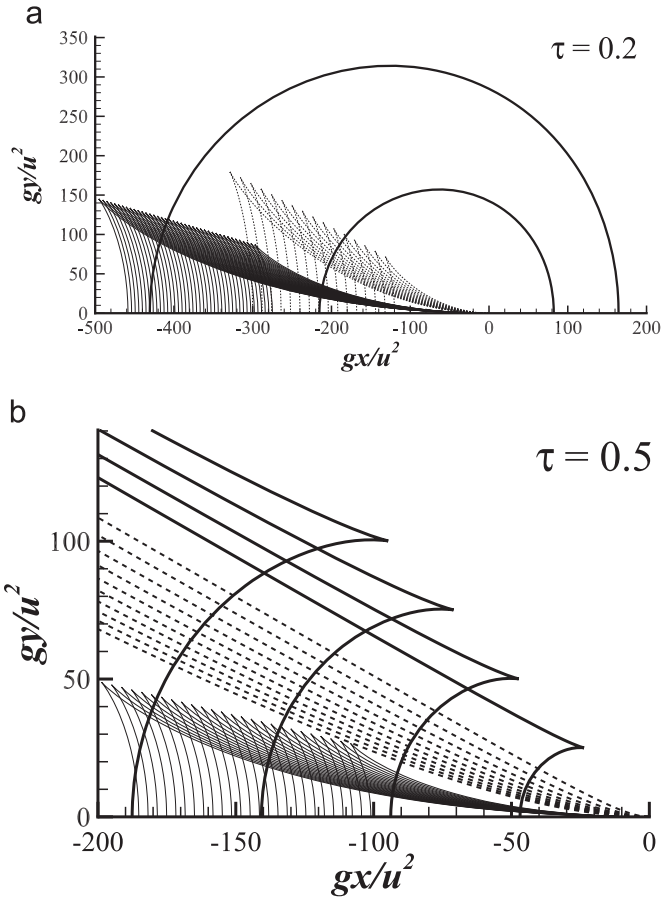

Fig. 2. Far-field wave patterns for a translating and pulsating source point located at (0, 0, z'), $z' < 0$. (a) τ=0.2; and (b) τ=0.5.

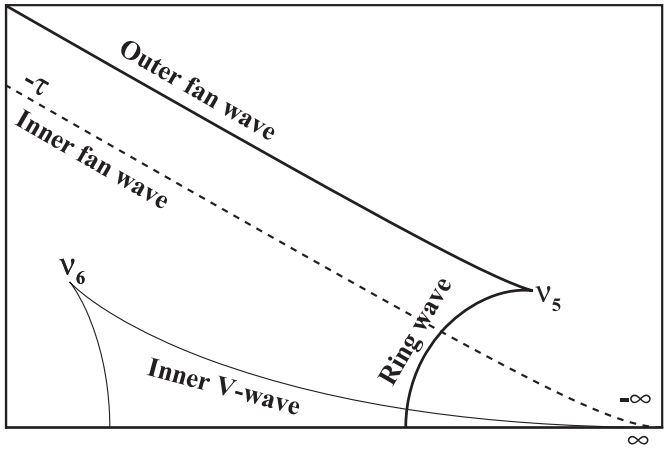

Fig. 3. Typical wave patterns for the case of $\tau > 0.25$.

not exist, since the ring waves could cover the entire computational domain. Therefore, in ship-to-ship problem, the minimum spacing cannot be identified and we are only concerned with the case of $\tau > 0.25$ in the present study.

Fig. 3 shows the typical wave patterns at $\tau > 0.25$. It can be observed that both of the ring waves and inner V waves have a cusp, which corresponds to the semi-wedge angle. Let's denote the coordinates of these cusps as (x_r, y_r) and (x_i, y_i) respectively, the corresponding semi-wedge angles can be written as

$$\theta_r = \tan^{-1}(-|y_r|/x_r) = \tan^{-1}\left[-\frac{\sqrt{(\nu_5-\tau)^4-\nu_5^2}}{2(\nu_5-\tau)^3-\nu_5}\right]$$
$$\theta_i = \tan^{-1}(-|y_i|/x_i) = \tan^{-1}\left[-\frac{\sqrt{(\nu_6-\tau)^4-\nu_6^2}}{2(\nu_6-\tau)^3-\nu_6}\right] \quad (15)$$

The values of ν_5 and ν_6 can be found in Noblesse and Hendrix (1992) as

$$\nu_{5,6} = -\frac{\sqrt{2-c+\sqrt{(1-2c)^2+48\tau^2}}}{2} \pm \left(\tau+\sqrt{1+c}/2\right) \quad (16)$$

where

$$c = (16\tau^2-1)^{1/3}\left[(1+4\tau)^{1/3}+(1-4\tau)^{1/3}\right]/2 \quad (17)$$

It should also be noted that as $\kappa_i \to -\tau$, the corresponding semi-wedge angle for the inner fan wave could be expressed as

$$\theta_f = \tan^{-1}\left[(-1)^{j-1}\frac{1}{\sqrt{16\tau^2-1}}\right] \quad (18)$$

The semi-wedge angles defined by Eqs. (15) and (18) are depicted in Fig. 4. The semi-wedge angle of the outer V waves is also presented. The expression of θ_o is the same as that of θ_r, as defined in Eq. (15). It should be noted that θ_o only exists at $\tau < 0.25$, while θ_r and θ_f exists at $\tau > 0.25$. The semi-wedge angle of the inner V waves exists at the entire range of τ. It can also be observed from Fig. 4 that at τ=0, the semi-wedge angles of the outer and inner V waves merge together as Kelvin wedge 19.47°. When it refers to ship-to-ship problem, as shown in Fig. 1, two values of τ are of particular interest: τ=0.272 (the analytical expression is $\sqrt{2/27}$, which can be found in Chen and Noblesse (1998)) and τ=1.62. At $\tau < 0.272$, the semi-wedge angle $\theta_r > 90°$. In this case, the hydrodynamic interactions between two ships are inevitable and the minimum spacing could not exist. Another critical case is τ=1.62. As $\tau > 1.62$, the semi-wedge angle $\theta_r < 19.47°$. In this case, the hydrodynamic interactions and the minimum spacing are dominated by the steady waves. The quiescent region could exist outside the Kelvin wedge. In the range of $0.272 < \tau < 1.62$, the quiescent region is deterred by θ_r, since θ_i and θ_f are confined within the semi-wedge angle of the ring waves.

From Fig. 1, the minimum spacing between two ships with the same forward speed can easily be obtained. Let's denote the length of the larger and smaller ships as L_a and L_b respectively, the minimum spacing between two ships can be written as

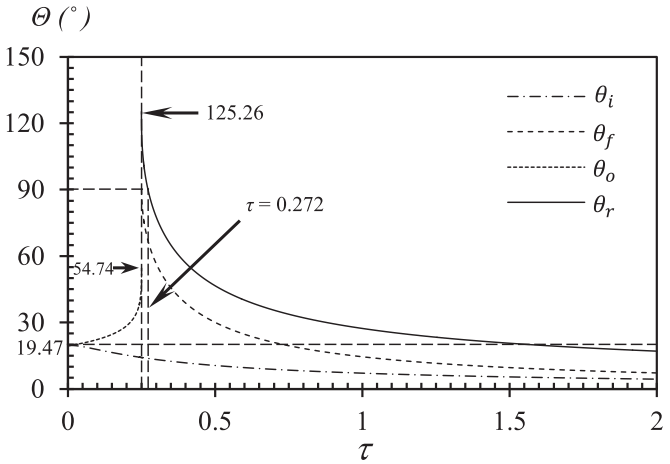

Fig. 4. Semi-wedge angles: θ_r, ring wave system ($\tau > 0.25$); θ_o, outer V wave system ($\tau < 0.25$); θ_i, inner V wave; θ_f, fan wave system ($\tau < 0.25$).

$$d = \frac{1}{2}(L_a + L_b)\tan(\theta) \tag{19}$$

Considering θ_i and θ_f are confined within the semi-wedge angle θ_r, by substituting Eq. (15) into Eq. (19), the dimensionless minimum spacing can be written as

$$d/L_a = \begin{cases} \infty, & (\tau \le 0.272) \\ \dfrac{1}{2}(1+\delta)\dfrac{\sqrt{(\nu_5-\tau)^4 - \nu_5^2}}{2(\tau-\nu_5)^3 + \nu_5}, & (0.272 < \tau < 1.62) \\ \dfrac{1}{2}(1+\delta)\tan(19.47^\circ), & (\tau \ge 1.62) \end{cases} \tag{20}$$

where $\delta = L_b/L_a$ is the ratio of the length of Ship_b to Ship_a, and ν_5 is defined in Eq. (16). From Eq. (20), it can be seen that the dimensionless minimum spacing is only determined by δ and τ. Fig. 5 shows the dimensionless minimum spacing with different δ values. It can be observed that as the ratio of the length of Ship_b to Ship_a increases, the distance between the two ships must be increased to minimize the hydrodynamic interactions.

3. Numerical validations

In order to validate the present assumption, we used MHydro, which is based on 3-D Rankine source panel method, to investigate the hydrodynamic properties of the floating bodies. Yuan et al. (2015a, 2014a) gave the details about using MHydro to solve the ship-to-ship with forward speed problem. The method developed and the results obtained have been validated by experimental measurements. The same method and numerical programme will be used in the present study, and only some general descriptions about the numerical methodology will be summarized here.

3.1. Numerical methodology

The corresponding right-handed coordinate systems are shown in Fig. 6. The body coordinate systems o_a-$x_a y_a z_a$ and o_b-$x_b y_b z_b$ are fixed on Ship_a and Ship_b respectively with their origins on the mean free surface, coinciding with the corresponding centre of gravity (CoG) in respect to x and y coordinates when both of the ships are at their static equilibrium positions. o_a-z_a and o_b-z_b are both positive upward. The inertia coordinate system o-xyz with origin located on the calm free surface coincides with o_a-$x_a y_a z_a$ when the ship has no unsteady motions. O-XYZ is the earth-fixed coordinate system with its origin located on the calm free surface

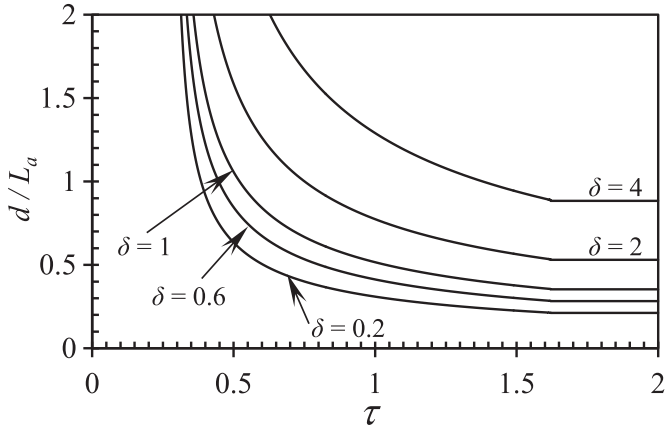

Fig. 5. Dimensionless minimum spacing between two advancing ships at δ=0.2, 0.6, 1, 2, and 4.

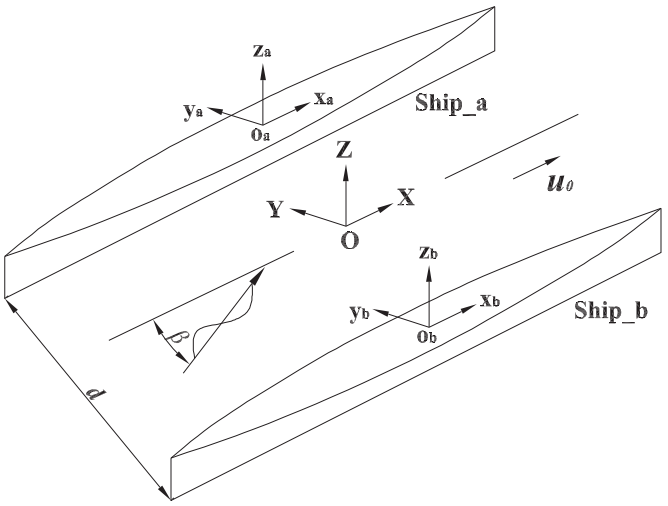

Fig. 6. An example vessels and coordinate system.

and OZ axis positive upward. The incident wave direction is defined as the angle between the wave propagation direction and X-axis. β=180° corresponds to head sea; β=90° corresponds to beam sea. d denotes the transverse distance between two ships while u_0 is the forward speed. In the computation, the motions and forces of Ship_a and Ship_b are concerted to the local coordinate system in which the origin is at the centre of gravity of each ship.

It is assumed that the surrounding fluid is inviscid and incompressible, and that the motion is irrotational, the total velocity potential exists which satisfies the Laplace equation in the whole fluid domain. Let t denote time and $\vec{\mathbf{x}} = (x, y, z)$ the position vector. The velocity potential provides a description of the flow as

$$\psi(\vec{\mathbf{x}}, t) = u_0\left[\varphi_s(\vec{\mathbf{x}}) - x\right] + \mathrm{Re}\sum_{j=1}^{6}[\eta_j^a \varphi_j^a(\vec{\mathbf{x}})e^{-i\omega_e t} + \eta_j^b \varphi_j^b(\vec{\mathbf{x}})e^{-i\omega_e t}] + \mathrm{Re}[\eta_0\varphi_0(\vec{\mathbf{x}})e^{-i\omega_e t}] + \mathrm{Re}[\eta_7\varphi_7(\vec{\mathbf{x}})e^{-i\omega_e t}], \quad j = 1, 2, \ldots, 6 \tag{21}$$

where φ_s is the steady potential and it is neglected in the present study; φ_j^a and φ_j^b (j=1,2,…,6) are the spatial radiation potentials in six degrees of freedom corresponding to the oscillations of Ship_a and Ship_b respectively and η_j (j=1,2,…6) is the corresponding motion amplitudes (η_1, surge; η_2, sway; η_3, heave; η_4, roll; η_5, pitch; η_6, yaw); η_7=η_0 is the incident wave amplitude; φ_7 is the spatial diffraction potential; φ_0 is the spatial incident wave potential and ω_e is the encounter frequency. Generally, the body boundary conditions can be treated separately by the diffraction and radiation problems as follows:

1) Body boundary conditions for the diffraction problem

$$\frac{\partial\varphi_7}{\partial n} = -\frac{\partial\varphi_0}{\partial n}\Big|_{S_a} \tag{22}$$

$$\frac{\partial\varphi_7}{\partial n} = -\frac{\partial\varphi_0}{\partial n}\Big|_{S_b} \tag{23}$$

2) Body boundary conditions for the radiation problem (Ship_a is oscillating while Ship_b is fixed)

$$\frac{\partial\varphi_j^a}{\partial n} = -i\omega_e n_j^a + u_0 m_j^a\Big|_{S_a} \tag{24}$$

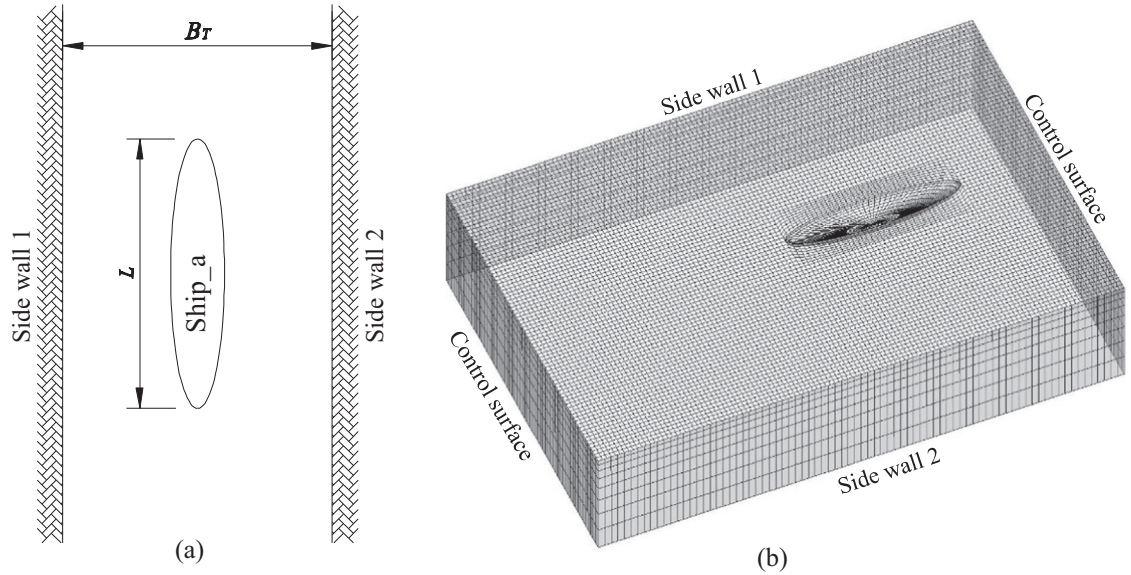

Fig. 7. A single ship advancing in a towing tank with two vertical side walls. (a) Model test condition; (b) panel distribution and computational domain of numerical model. For the numerical model, there are 6324 panels distributed on the half of the computational domain: 404 on the body surface, 4800 on the free surface, 480 on the control surfaces and 640 on the vertical side walls. The computational domain is truncated at L upstream, 2L downstream.

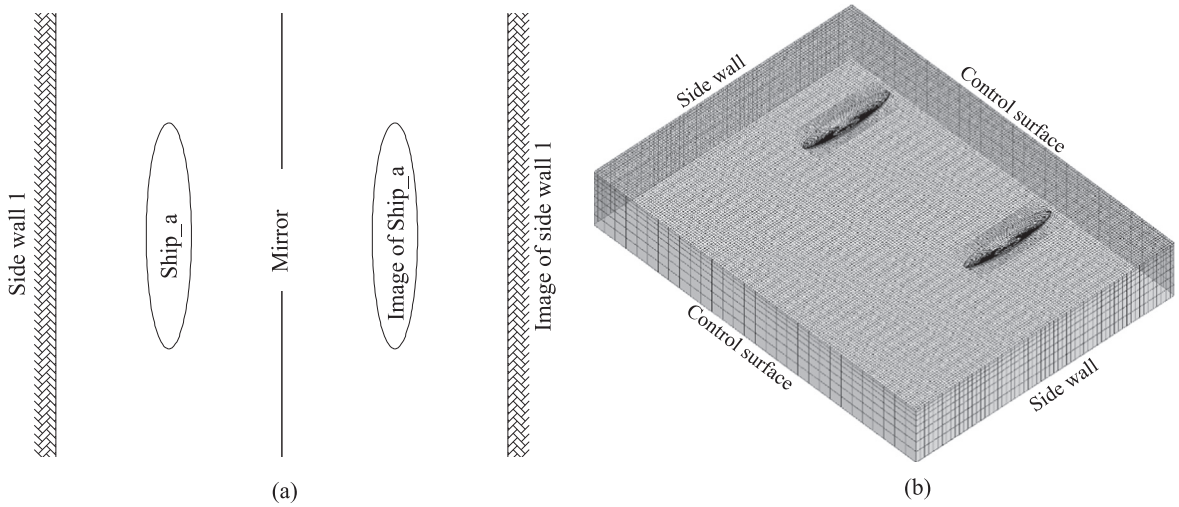

Fig. 8. (a) Image method of side wall problem; (b) panel distribution and computational domain of ship-to-ship problem. For the numerical model of ship-to-ship problem, there are 22,256 panels distributed on the entire computational domain: 808 on each body surface, 19,200 on the free surface and 960 on the vertical side walls and the rest on the control surface. The computational domain is truncated at L upstream, 2L downstream.

$$\frac{\partial \varphi_j^a}{\partial n} = 0|S_b \tag{25}$$

3) Body boundary conditions for the radiation problem (Ship_b is oscillating while Ship_a is fixed)

$$\frac{\partial \varphi_j^b}{\partial n} = -i\omega_e n_j^b + u_0 m_j^b|S_b \tag{26}$$

$$\frac{\partial \varphi_j^b}{\partial n} = 0|S_a \tag{27}$$

where $\vec{n} = (n_1, n_2, n_3)$ is the unit normal vector directed inward on body surface. The m_j denotes the j-th component of the so-called m-term and for the slender vessels, it can be expressed by

$$(m_1, m_2, m_3) = (0, 0, 0)$$
$$(m_4, m_5, m_6) = (0, n_3, -n_2) \tag{28}$$

The free surface boundary for both diffraction and radiation problem can be written as:

$$g\frac{\partial \varphi_j}{\partial z} - \omega_e^2 \varphi_j + 2i\omega_e u_0 \frac{\partial \varphi_j}{\partial x} + u_0^2 \frac{\partial^2 \varphi_j}{\partial x^2} = 0, \quad j = 1, 2, ...7 \tag{29}$$

The radiation condition for both diffraction and radiation problem is satisfied by using Sommerfeld radiation condition with forward speed correction, which can be found by Yuan et al. (2014a, 2014b) and Das and Cheung (2012).

Once the unknown diffraction potential φ_7 and radiation potential φ_j are solved, the time-harmonic pressure can be obtained from Bernoulli's equation:

$$p_j = \rho \eta_j \left(i\omega_e \varphi_j + u_0 \frac{\partial \varphi_j}{\partial x} \right), \; j = 0, \; 1, \ldots, \; 7 \tag{30}$$

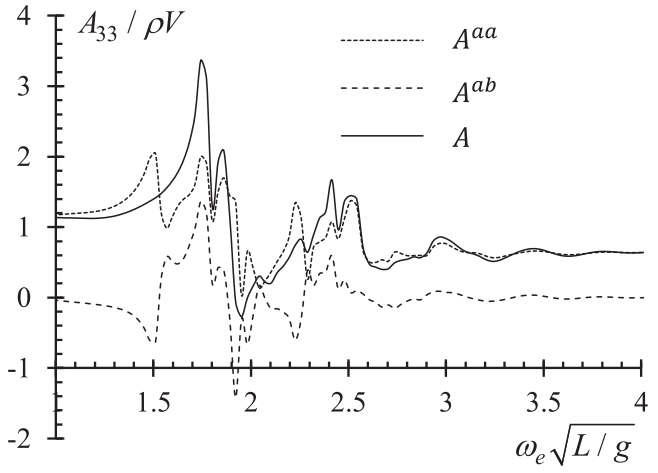

Fig. 9. Heave added mass and its components obtained by using superposition method.

where ρ is the fluid density. The hydrodynamic forces produced by the oscillatory motions of the vessel in the six degrees of freedom can be derived from the radiation potentials as given in the following (Yuan et al., 2015a)

$$F_i^{Ra} = \sum_{j=1}^{6} \iint_{S_a} p_j^a n_i dS \cdot (\eta_j^a + \eta_j^b) = \sum_{j=1}^{6} \left[\omega_e^2 A_{ij}^{aa} + i\omega B_{ij}^{aa}\right]\eta_j^a + \sum_{j=1}^{6} \left[\omega_e^2 A_{ij}^{ab} + i\omega B_{ij}^{ab}\right]\eta_j^b,\ i = 1,\ 2, \ldots,\ 6 \tag{31}$$

$$F_i^{Rb} = \sum_{j=1}^{6} \iint_{S_b} p_j^b n_i dS \cdot (\eta_j^a + \eta_j^b) = \sum_{j=1}^{6} \left[\omega_e^2 A_{ij}^{ba} + i\omega_e B_{ij}^{ba}\right]\eta_j^a + \sum_{j=1}^{6} \left[\omega_e^2 A_{ij}^{bb} + i\omega_e B_{ij}^{bb}\right]\eta_j^b,\ i = 1,\ 2, \ldots,\ 6 \tag{32}$$

where A_{ij}^{aa} is the added mass of Ship_a in i-th mode which is induced by the motion of Ship_a in j-th mode; A_{ij}^{ab} is the added mass of Ship_a in i-th mode which is induced by the motion of Ship_b in j-th mode; A_{ij}^{ba} is the added mass of Ship_b in i-th mode which is induced by the motion of Ship_a in j-th mode; A_{ij}^{bb} is the added mass of Ship_b in i-th mode which is induced by the motion of Ship_b in j-th mode; B is the damping and the definition of the subscripts used are the same as those of the added mass.

The wave excitation forces can be obtained by the integration of incident and diffraction pressure as

$$F_i^{Wa} = \iint_{S_a} (p_0 + p_7) n_i dS \tag{33}$$

$$F_i^{Wb} = \iint_{S_b} (p_0 + p_7) n_i dS \tag{34}$$

The wave elevation on the free surface then can be obtained from the dynamic free surface boundary condition in the form

$$\zeta_j = \frac{i\omega_e}{g}(\eta_j^a \varphi_j^a + \eta_j^b \varphi_j^b) + \frac{1}{g}\nabla(\varphi_s - u_0 x)\cdot\nabla(\eta_j^a \varphi_j^a + \eta_j^b \varphi_j^b) = \zeta_{Rj} + i\zeta_{Ij},\quad j = 0,\ 1, \ldots,\ 7 \tag{35}$$

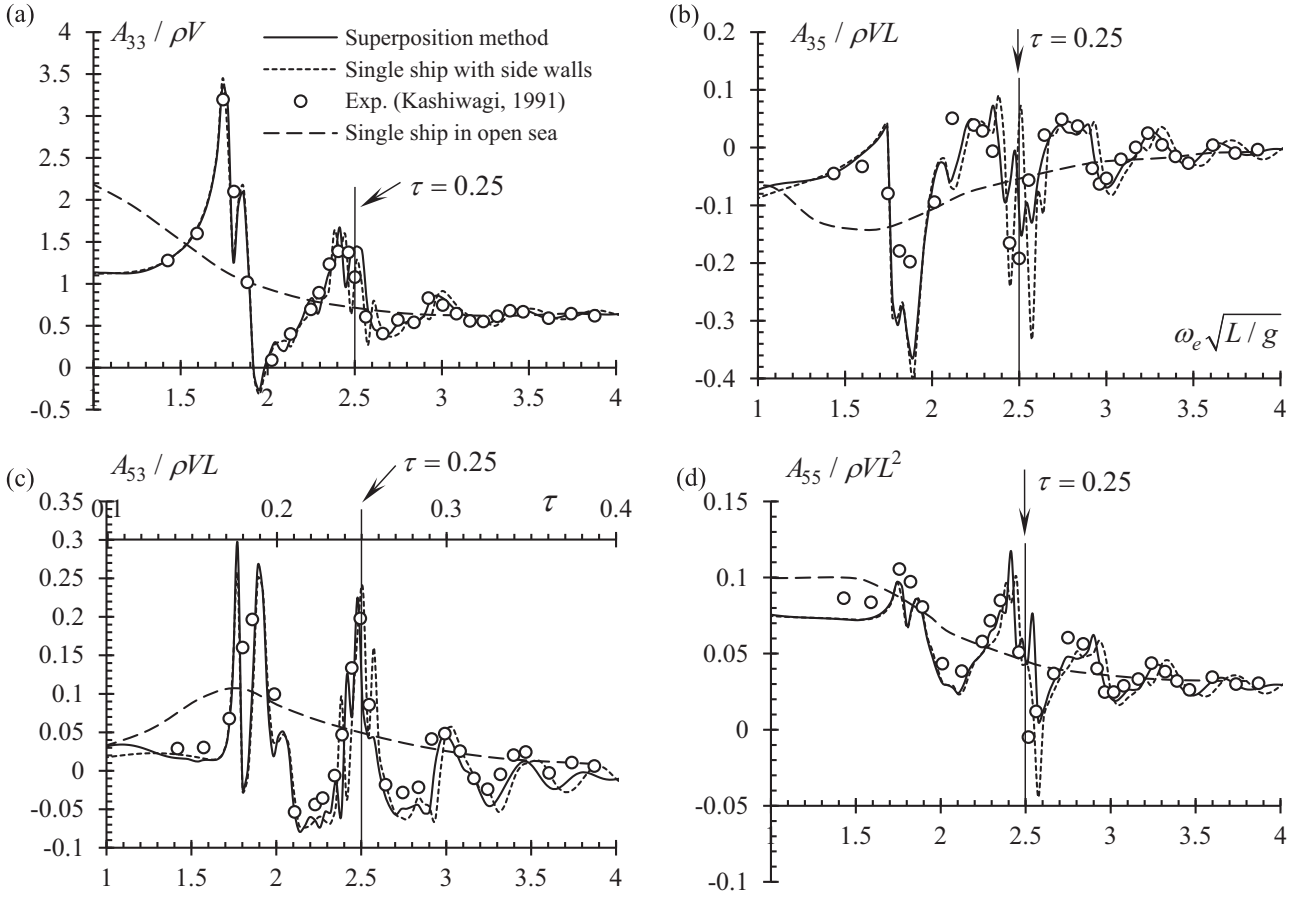

Fig. 10. Added mass of a half-immersed prolate spheroid of $B/L=1/5$ in waterway of $B_T/L=2.0$ ($F_n=0.1$). (a) Heave-induced heave added mass; (b) pitch-induced heave added mass; (c) heave-induced pitch added mass; and (d) pitch-induced pitch added mass.

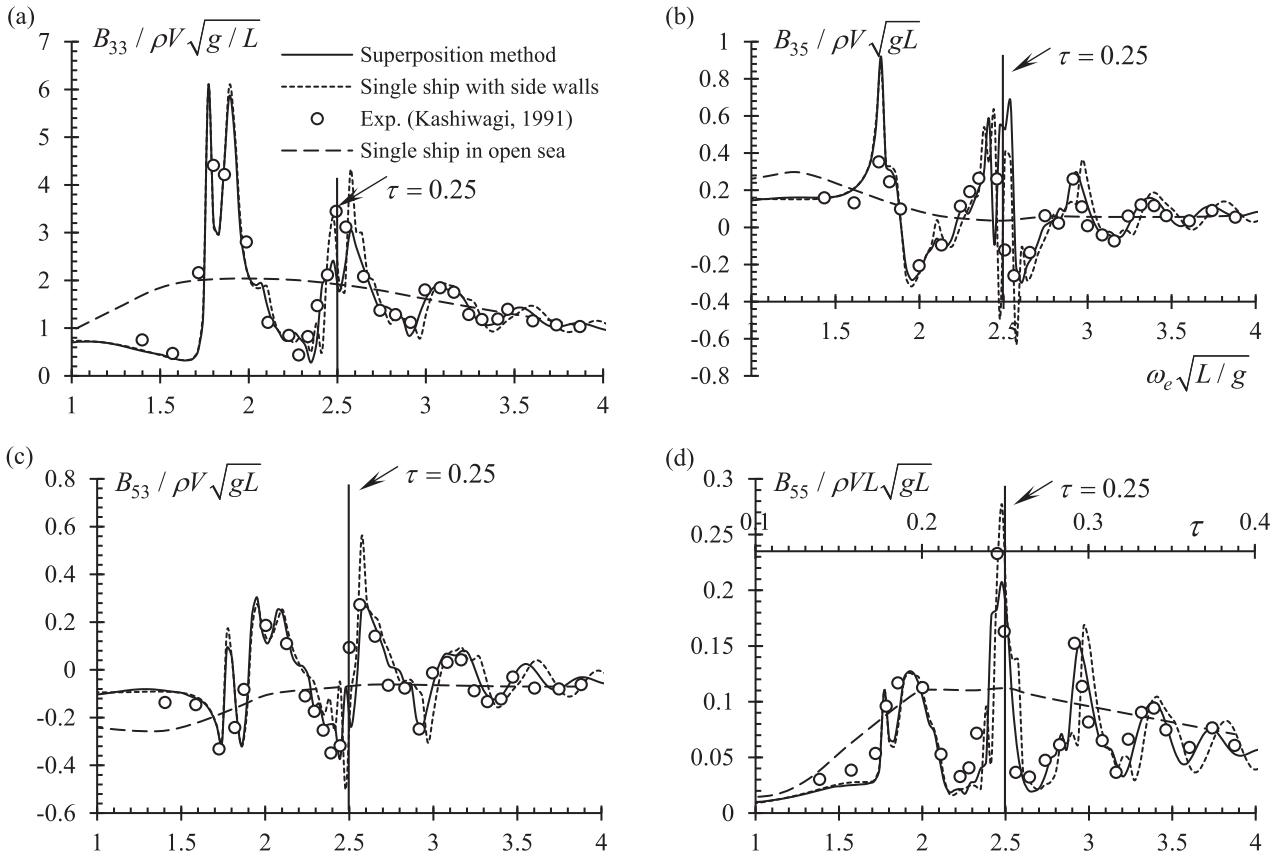

Fig. 11. Damping of a half-immersed prolate spheroid of $B/L=1/5$ in waterway of $B_T/L=2.0$ ($F_n=0.1$). (a) Heave-induced heave damping; (b) pitch-induced heave damping; (c) heave-induced pitch damping; and (d) pitch-induced pitch damping.

where ζ_{Rj} is the real part of j-th model, and ζ_{Ij} is the imaginary part.

3.2. Validations

Before we carry out massive numerical calculations, a rigorous validation of the numerical programme should be conducted. Unfortunately, due to the complexities involved in the model test of two ships advancing in waves, only very limited model test data is available from the published resources. McTaggart et al. (2003) and Li (2007) presented some experimental data of ship-to-ship with forward speed in waves based on their model tests carried out at the Institute for Marine Dynamics (IMD) in St. John's, Newfoundland. Similar work was also conducted by Ronæss (2002) and her model test was carried out at the Marine Technology Centre in Trondheim, Norway. More recently, Xu and Dong (2013) carried out experimental tests to measure the wave loads and the free motions for a pair of side-by-side arranged ship models advancing with an identical speed in head regular waves. The validations of the present numerical programme MHydro against the model test results from McTaggart et al. (2003) and Ronæss (2002) can be found in Yuan et al. (2015a, 2014a). In their validations, the heave and pitch RAOs of both ships were well predicted. However, they failed to predict the roll motion due to the viscus effects. In the present study, we are not going to make any efforts to calculate the motion RAOs. One of the reason has been demonstrated above as the viscus effect. Besides, the motion responses are not able to reflect the hydrodynamic interactions directly. For example, the motion responses are also determined by the mass and restoring force matrix, as well as the incident wave forces. And in most of the frequency range, the motion responses are dominated by these components rather than the radiation and diffraction forces. Therefore, in the present study, we are particularly interested in the hydrodynamic coefficients, which can directly reflect the hydrodynamic interaction. Without consideration of speed effects, Kashiwagi et al. (2005) published his model test results of the diffraction and radiation forces of a rectangular box and Wigley hull interacted in waves. We used his model test results to validate MHydro in zero speed case (Yuan et al., 2015a). Taking the forward into consideration, Kashiwagi and Ohkusu (1989, 1991) conducted model test to investigate the ship and side wall interference. Kashiwagi (1993a, 1993b) also published some experimental results of the wave exciting forces and hydrodynamic coefficients about a catamaran. In the present study, Kashiwagi and Ohkusu (1991) model test results of side wall effects will be used here to validate the numerical programme. Based on the assumption that the ships involved in ship-to-ship problem are arranged side-by-side and the geometry and the speed of the ships are exactly the same, a single ship with side walls problem shown in Fig. 7 can be replaced by ship-to-ship problem shown in Fig. 8. The existence of side wall 2 in Fig. 7(a) is equivalent of replacing it with a mirror. The images of side wall 1 and Ship_a make the single ship with side walls problem exactly the same with ship-to-ship problem shown in Fig. 8(b). Therefore, the superposition method used in the present study can be validated through the model test of side wall effects conducted by Kashiwagi (1991).

The model used here is a half-immersed prolate spheroid of length $L=2.0$ m and breadth $B=0.4$ m. The model test was conducted in the towing tank (60 m length, 4 m breadth, 2.3 m in depth) of Nagasaki Institute of Applied Science. The model was

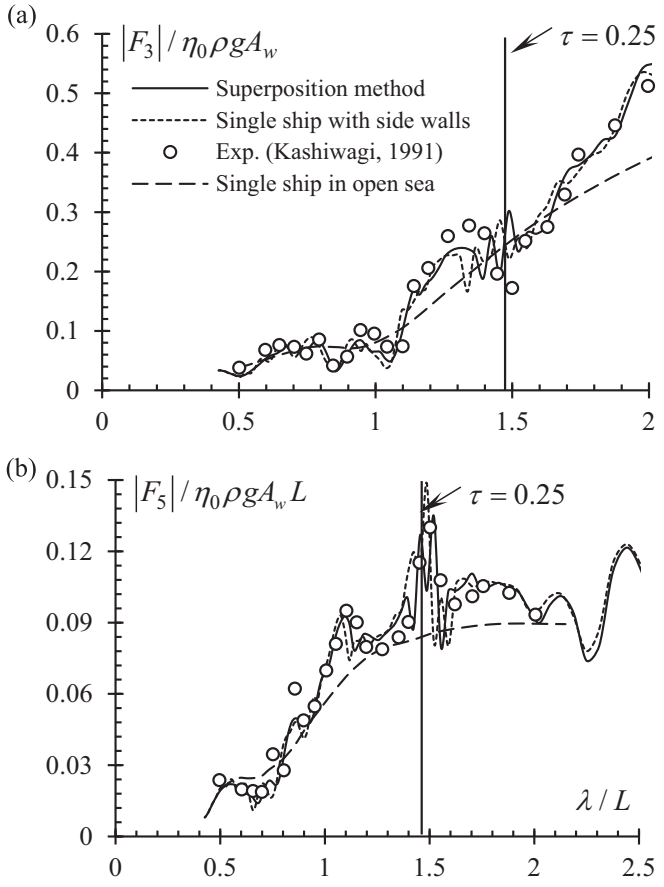

Fig. 12. Wave exciting forces of a half-immersed prolate spheroid of $B/L=1/5$ in waterway of $B_T/L=2.0$ ($F_n=0.1$). (a) Heave wave exciting force; and (b) pitch wave exciting moment. A_w is the water plane area.

Table 1
Main dimensions of Wigley III hull.

Length, L (m)	3
Breadth, B (m)	0.3
Draught, D (m)	0.1875
Displacement, V (m^3)	0.078
Centre of rotation above base, KR (m)	0.1875
Centre of gravity above base, KG (m)	0.17
Radius of inertia for pitch, k_{yy} (m)	0.75

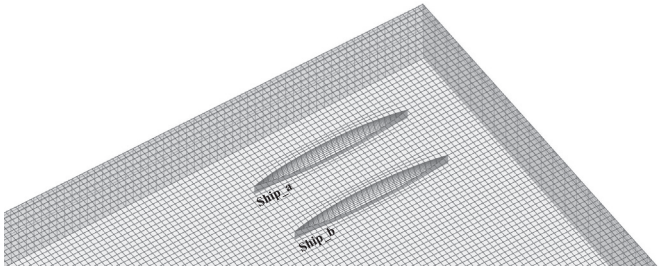

Fig. 13. The computational domain of the numerical model. There are 12,090 panels distributed on the entire computational domain: 600 on each body surface of Wigley hull, 9450 on the free surface and 1440 on the control surface. The computational domain is truncated at L upstream, 2L downstream, 0.5L sideways in the portside and 3L sideways in the starboard referred to Ship_a.

advancing at a Froude number $F_n=0.1$ in the waterway of $B_T/L=2.0$, where B_T is the transverse distance between the ship and side wall. Two numerical simulations are performed by using MHydro. The first simulation adopts the same situation as that

Table 2
Main parameters for each case.

	Speed u_0 (m/s)	Spacing d (m)	Staggered distance s (m)	Parameter τ	Semi-wedge angle θ (°)
Case 1	1.22	1.2	0	0.88	30
Case 2	1.22	2.2	0	0.88	30
Case 3	1.22	2.2	1.5	0.38	30
Case 4	0.636	2.2	0	0.38	60

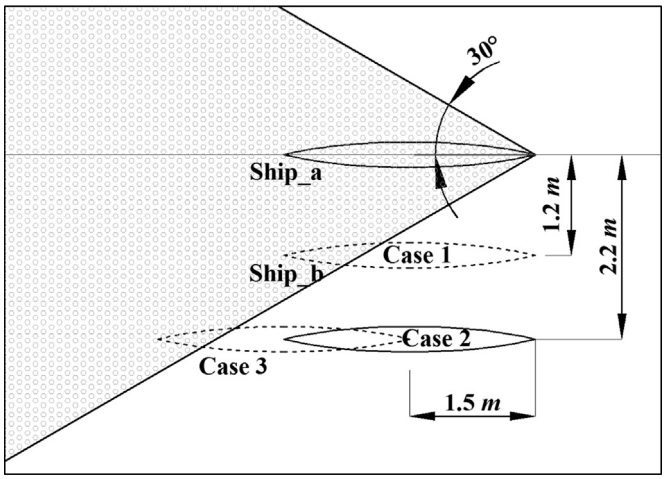

Fig. 14. Configurations of Cases 1–3.

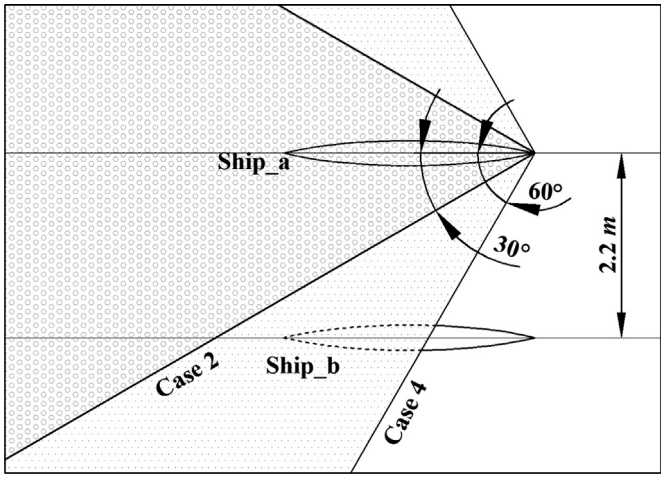

Fig. 15. Sketch of Cases 2 and 4.

Table 3
Wave exciting forces on both ships of Cases 1–3.

	Surge	Sway	Heave	Roll	Pitch	Yaw
Single ship ($u_0=1.22$ m/s)	0.056	0.002	0.168	0.00008	0.28	0.001
Case 1	0.061	0.06	0.157	0.00284	0.299	0.054
Case 2	0.056	0.005	0.17	0.00027	0.279	0.005
Case 3 (Ship_a)	0.056	0.002	0.168	0.00008	0.279	0.001
Case 3 (Ship_b)	0.051	0.046	0.153	0.00224	0.267	0.042

used in the model test and the panel distribution and computational domain of numerical model is shown in Fig. 7(b). The corresponding numerical results are referred as 'Single ship with side walls' hereafter. The second simulation is based on superposition method and two ships with side walls are modelled. The panel distribution and computational domain of numerical model is shown in Fig. 8(b), and the corresponding numerical results are

Table 4
Wave exciting forces on both ships of Cases 2 and 4.

	Surge	Sway	Heave	Roll	Pitch	Yaw
Single ship (u_0=0.636 m/s)	0.055	0.002	0.172	0.00013	0.277	0.002
Case 2	0.056	0.005	0.17	0.00027	0.279	0.005
Case 4	0.05	0.06	0.161	0.0024	0.263	0.045

referred as 'Superposition method'. It should be noted that in both of the numerical simulations, the mesh size and the truncation of the free surface are consistent.

The hydrodynamic coefficients (for example, the added mass A) obtained from the model tests and numerical simulation of single ship represent the total hydrodynamic coefficients of Ship_a directly. However, the hydrodynamic coefficients of Ship_a obtained by using the superposition method consist of two components which can be written as $A=A^{aa}+A^{ab}$, where A^{aa} represents the added mass of Ship_a when Ship_a is oscillating while Ship_b is fixed, and A^{ab} represents the added mass of Ship_a when Ship_a is fixed while Ship_b is oscillating. A^{aa} can be obtained by solving the boundary value problem from Eqs. (24) and (25), while A^{ab} can be obtained by solving the boundary value problem from Eqs. (26) and (27). The heave added mass and its components are shown in Fig. 9. A^{ab} represents the effect of side wall 1 and it is the main contribution of the negative added mass at certain frequencies.

Figs. 10 and 11 show the hydrodynamic coefficients. Generally, the agreement between 'Superposition method' and 'Single ship with side walls' is satisfactory. Some discrepancies between 'Superposition method' and 'Single ship with side walls' can be observed at high frequency range, which can be attributed to the numerical dispersion and damping (Kim et al., 2005) introduced by the constant panel method. The numerical dispersion and damping are mainly determined by the parameter ε ($\varepsilon=\lambda/dx$, where λ is the wavelength and dx is the mesh size on the free surface). The numerical dispersion and damping are not noticeable at $\varepsilon>20$. However, as $\varepsilon<20$, the numerical dispersion and damping become evident. In the present study, the wavelength λ is small at high frequency range. But as the unified mesh is applied, the parameter ε becomes very small. Therefore, the numerical dispersion and damping are inevitable. The numerical dispersion and damping becomes even more evident in ship-to-ship problem, since the free surface is larger than that in a narrow tank. The waves produced by Ship_a have to propagate a long distance until they strike Ship_b, and during this propagation, the numerical dispersion and damping occurs. However, in single ship with two side walls problem (the mesh size on the free surface is exactly the same as that in ship-to-ship problem), the free surface is smaller. The reflected waves from the wall only travel a short distance, then they can strike the ship model. Therefore, the numerical dispersion and damping are not as obvious as that in ship-to-ship problem. The numerical dispersion and damping modify the wavelength and amplitude during the propagation of the radiated waves (or reflected waves) and this is the main reason for the different phase and amplitude between the results obtained by two numerical methods at high frequency range. There are still some discrepancies that are found at $0.24<\tau<0.27$, which can be attributed to the complicated waves trapped in the narrow gap between the side walls in the vicinity of the critical frequency. However, the general agreement between 'Superposition method' and 'Single ship with side walls' is still satisfactory which indicates that the present method is capable to predict the hydrodynamic interactions between two ships with the same speed. As the parameter $\tau<0.25$ $\left(\omega_e\sqrt{L/g}<2.5\right)$, the hydrodynamic coefficients (radiation forces) fluctuate violently away from the open sea results. As $\tau<0.25$, the radiated waves from the mirrored spheroid (or the reflected waves from the side walls) can propagate to the domain where the spheroid is located and strike the spheroid. The agreement between the present calculations and experiments is very satisfactory even at parameter $\tau<0.25$, which indicates the radiation condition included in the present numerical programme MHydro is capable to predict the hydrodynamic properties of the advancing ships even at parameter $\tau<0.25$. As the parameter τ increases, the hydrodynamic coefficients gradually approach the open sea results and hydrodynamic interaction (or the side wall effects) trend to diminish. Fig. 12 shows the wave exciting forces of a half-immersed prolate spheroid of $B/L=1/5$ in waterway of $B_T/L=2.0$ ($F_n=0.1$). Both of the heave force and pitch moment agree well with the experimental measurements. A very large spike can be observed at $\lambda/L=1.47$, which corresponds to $\tau=0.25$. In the present study, we are particular interested in the range of $\tau>0.272$, where the semi-wedge angle θ exists and the minimum spacing can be determined by Eq. (20).

3.3. Case study

The validated numerical programme MHydro is used in this session to examine the reliability of the theoretical estimation of the minimum spacing. A series of case studies are designed here based on two identical Wigley III hulls advancing side by side in head waves with the same forward speed. Thus, δ in Eq. (20) is fixed at 1, and then the dimensionless minimum spacing in Eq. (20) is only determined by parameter τ. The main dimensions of Wigley III model is shown in Table 1. The computational domain and discretization of the boundaries is presented in Fig. 13.

The incident wavelength to ship length ratio of $\lambda/L=1$ in head sea corresponds to the critical conditions in ship design. In this case, the incident wave frequency $\omega_0=4.53$ rad/s. Four typical cases, as shown in Table 2, are investigated in the present study to verify our assumption. These cases can be divided into two categories, in order to make the comparisons conclusive. The first category involves Cases 1–3. The basic principle for this category is that the forward speed is fixed at the same value at $u_0=1.22$ m/s. Therefore, according to Fig. 4, the corresponding semi-wedge angle is 30°. But the positions of the ships are different. In Case 1, the spacing is 1.2 m, which means part of Ship_b is located in the wake region of Ship_a. In Case 2, the spacing is 2.2 m, which indicates that Ship_b is entirely located in the quiescent region of Ship_a. In Case 3, the spacing keeps the same as that in Case 2. But Ship_b is staggered at 1.5 m downstream. Thus, the stern of Ship_b will also be covered by Ship_a's wake. The configurations of the first category are depicted in Fig. 14. The second category involves in Cases 2 and 4. The basic principle for this category is that the positions of

Table 5
Added mass of Ship_b induced by the unit motion of Ship_a.

	$A_{22}{}^{ba}$	$A_{23}{}^{ba}$	$A_{26}{}^{ba}$	$A_{32}{}^{ba}$	$A_{33}{}^{ba}$	$A_{36}{}^{ba}$	$A_{52}{}^{ba}$	$A_{53}{}^{ba}$	$A_{62}{}^{ba}$	$A_{66}{}^{ba}$
Case 1	0.207	−0.148	0.04	0.185	−0.114	0.048	0.04	−0.027	−0.041	−0.003
Case 2	−0.011	0.007	−0.004	−0.002	0.002	−0.001	0	0	0.004	0.002
Case 3	−0.152	−0.09	−0.047	0.01	0.004	0.008	−0.002	−0.003	0.058	0.016
Case 4	0.337	−0.129	0.108	0.045	0.077	0.051	0.027	0.002	−0.12	−0.029

Table 6
Damping of Ship_b induced by the unit motion of Ship_a.

	B_{22}^{ba}	B_{23}^{ba}	B_{26}^{ba}	B_{32}^{ba}	B_{33}^{ba}	B_{36}^{ba}	B_{52}^{ba}	B_{53}^{ba}	B_{62}^{ba}	B_{66}^{ba}
Case 1	−1.177	0.713	−0.347	−0.32	0.169	−0.128	−0.059	0.024	0.408	0.107
Case 2	−0.025	0.009	−0.01	−0.019	0.01	−0.007	−0.006	0.003	0.009	0.003
Case 3	−0.834	−0.547	−0.205	0.536	0.331	0.151	0.117	0.075	0.222	0.046
Case 4	1.04	−1.02	0.119	1.082	−0.736	0.255	0.168	-0.151	-0.128	0.033

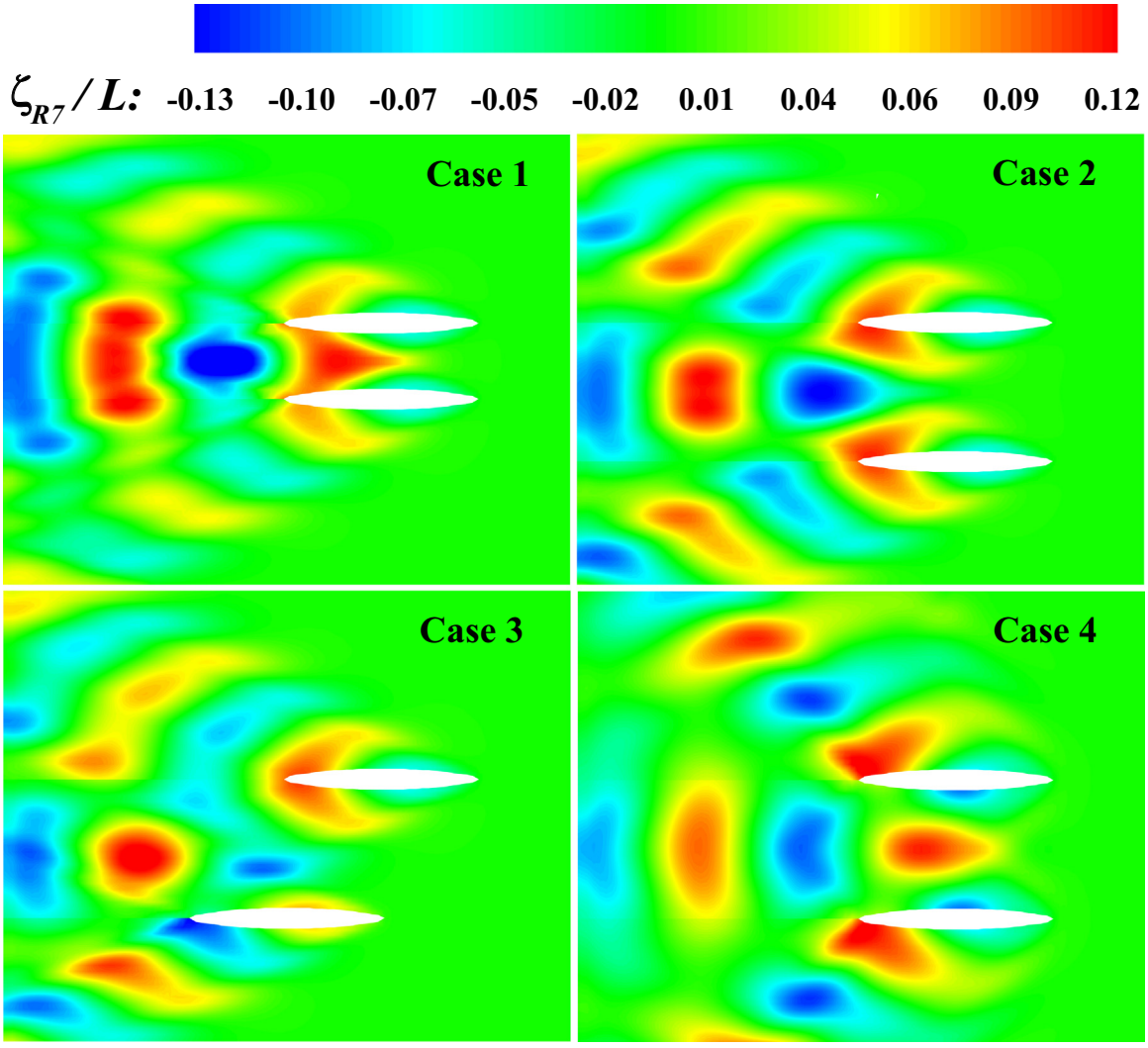

Fig. 16. Real part of diffracted waves of two ships advancing in head waves.

the ships in Case 4 are kept identical to that in Case 2, which has been described previously. The only difference between these two cases lies on the forward speed. In case 2, the forward speed is fixed at $u_0=1.22$ m/s and the corresponding semi-wedge angle is 30°. Therefore, Ship_b would be entirely located in the quiescent region of Ship_a. But in Case 2, the forward speed is $u_0=0.636$ m/s. According to Fig. 4, the corresponding semi-wedge angle is 60°, which means the major part of Ship_b would be located in Ship_a's wake. The sketch of Cases 2 and 4 is shown in Fig. 15.

3.3.1. Wave exciting forces

The results of the wave exciting forces of Cases 1–3 are shown in Table 3. The results of the single ship are also included for comparison. The non-dimensionalisation for surge, sway and heave is made by using $\eta_0 C_{33}$; the non-dimensionalisation for roll, pitch and yaw is made by using $\eta_0 K_0 C_{55}$, where η_0 is the incident wave amplitude, and C_{33} and C_{55} represent the restoring coefficients in heave and pitch direction respectively. In Cases 1 and 2, the wave exciting forces on both ships are the same. But in Case 3, the staggered configuration violates the symmetrical property of the flow field. As a result, the wave exciting forces of Ship_a and Ship_b are different, and they are listed individually in Table 3. In head wave condition, the best way to examine the hydrodynamic interactions is by calculating the sway, roll and yaw exciting forces. Theoretically, the sway, roll and yaw exciting forces of single ship must be zero due to the symmetrical characteristics of the incident flow and body surface. But in numerical simulation, these forces fluctuate around zero, which could attribute to the numerical errors. However, in Cases 1 and 3 (Ship_b), the wave exciting forces in sway, roll and yaw directions are very large. These forces on Ship_b are produced by the diffracted waves from Ship_a, since Ship_b in Cases 1 and 3 are partly located in the wake region of

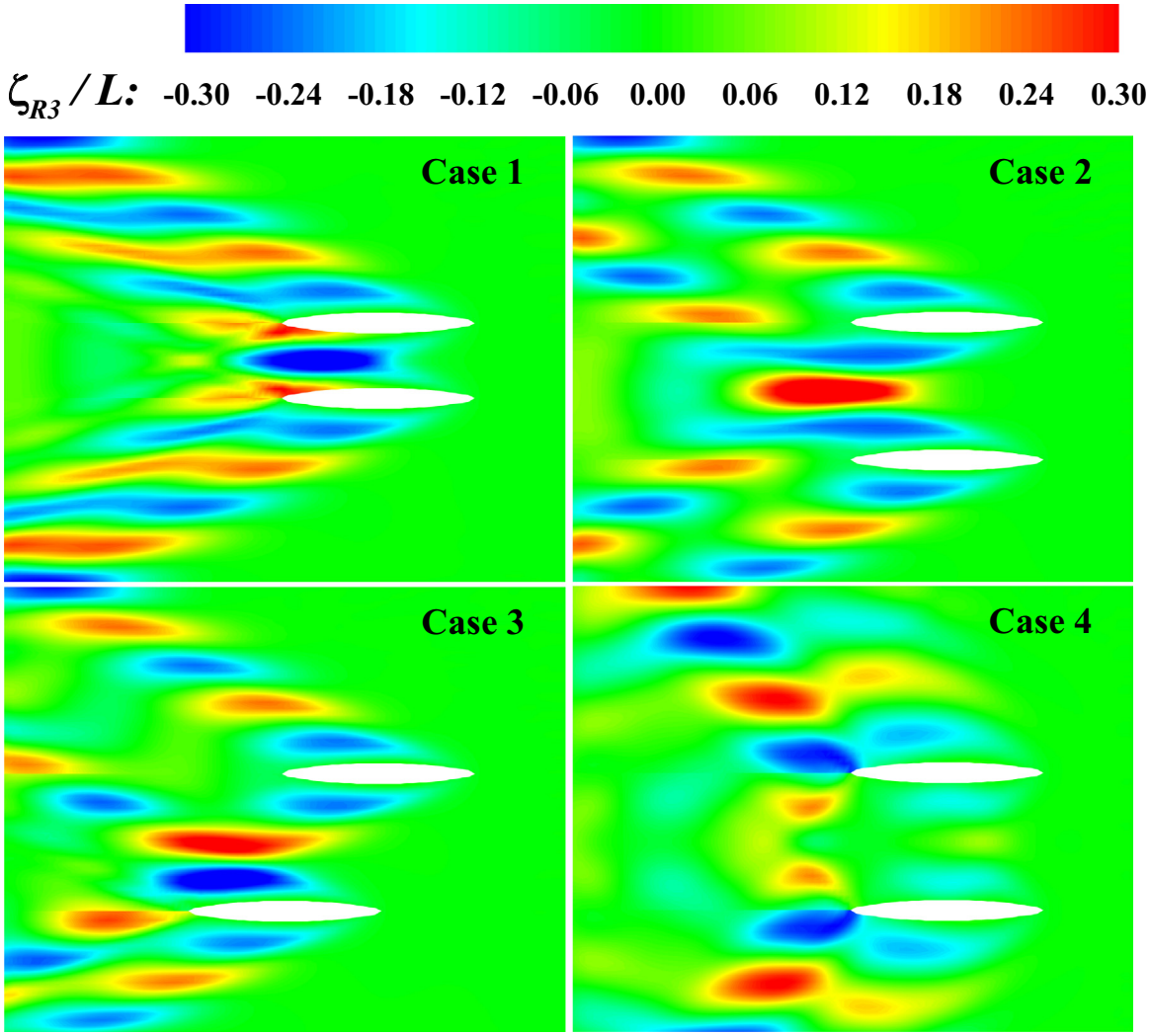

Fig. 17. Real part of radiated waves for unit heave motion of two ships advancing in head waves.

Ship_a. But in Case 2, the wave exciting forces in these three directions are very small, which indicates that the diffracted waves from Ship_a could hardly influence the flow field around Ship_b. Moreover, in Case 3, the wave exciting forces on Ship_a are almost identical to those of single ship case, which indicates that the flow field around Ship_a could not be disturbed by the existence of Ship_b. The above findings are consistent with our assumption, and it can be concluded that in head waves, if both of the ships are located at each other's quiescent region, the diffracted interactions can be minimized.

The comparisons in Table 3 are based on the same forward speed (the same semi-wedge angle). Table 4 presents some results with different forward speeds. Even though the configurations of Cases 2 and 4 are the same, the discrepancies between the calculated forces in sway, roll and yaw are significant. In Case 2, the diffracted waves produced by Ship_a are confined within a relatively smaller semi-wedge angle, and Ship_b is entirely located in the quiescent region. As a result, the wave exciting forces in sway, roll and yaw are very small. But as the forward speed decreases, the semi-angle becomes larger, and the quiescent region is shrunk. As a result, in Case 4, Ship_b will be partly covered by the diffracted wave field from Ship_a. Consequently, the wave exciting forces in sway, roll and yaw directions are significant, as shown in Table 4. These results also coincide with our theoretical assumption.

3.3.2. *Hydrodynamic coefficients*

The added mass and damping of Ship_b induced by the unit motion of Ship_a are presented in Tables 5 and 6 respectively. These hydrodynamic coefficients reflect the influence from the radiated waves due to the existence of the other ship. The non-dimensionalisation for added mass with subscript of 22, 23, 32, and 33 is made by ρV; the subscript of 26, 36, 52, 53 and 62 is made by ρLV; the subscript of 66 is made by ρL^2V. The non-dimensionalisation for damping with subscript of 22, 23, 32, and 33 is made by $\rho V\sqrt{g/L}$; the subscript of 26, 36, 52, 53 and 62 is made by $\rho VL\sqrt{g/L}$; the subscript of 66 is made by $\rho VL^2\sqrt{g/L}$. From the results of Case 2, it can be found that the radiated waves produced by the unit motion of Ship_a could hardly influence the hydrodynamic properties of Ship_b. While in the other three cases, the hydrodynamic interaction on Ship_b is significant due to the disturbance of the radiated waves from Ship_a. The above conclusions are consistent with our theoretical assumption, which indicates that if the ship is located in the quiescent region of the other ship, the hydrodynamic interactions could be minimized.

3.3.3. *Wave pattern*

Figs. 16 and 17 present the diffracted and radiated wave patterns for different cases. Because of the existence of Ship_a, the symmetrical property of the flow field around Ship_b in Cases 1, 3 and 4 is violated. In these cases, the diffracted or radiated waves

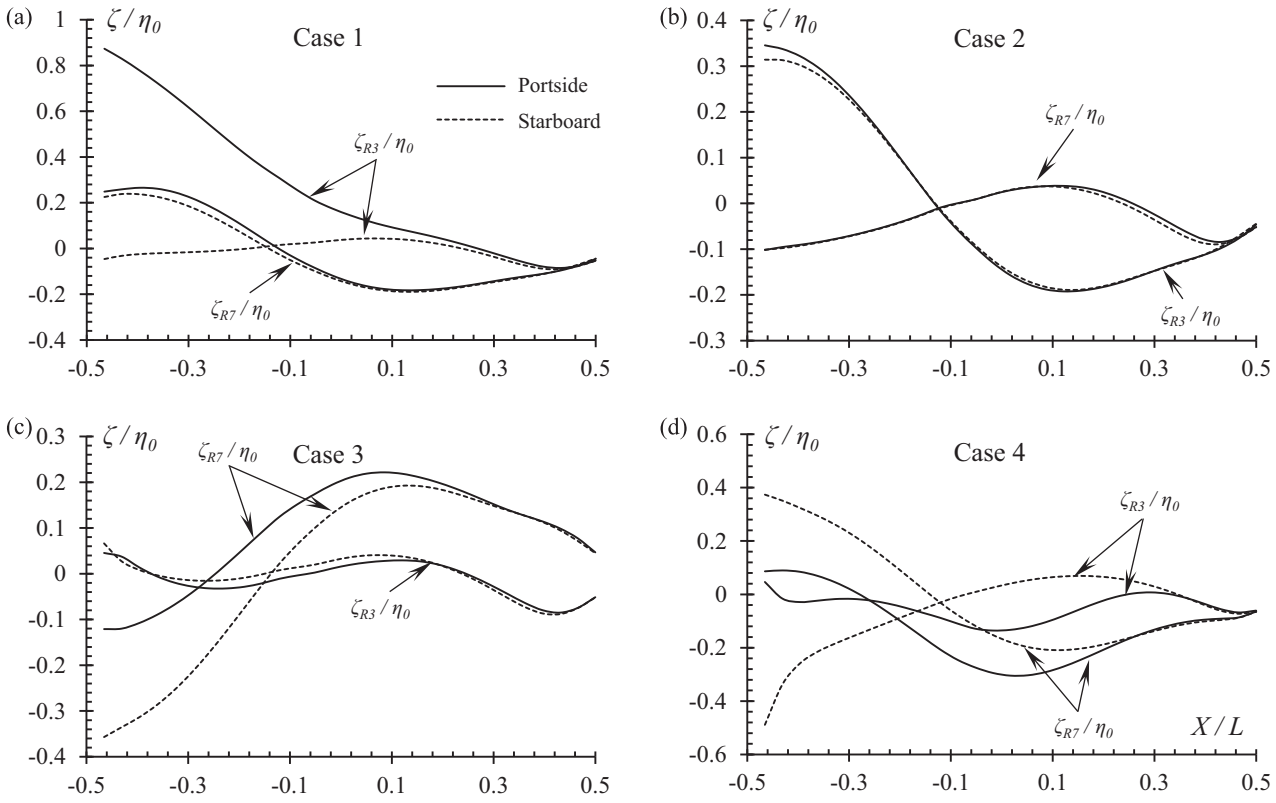

Fig. 18. Wave profiles (real part) at portside and starboard of Ship_b. (a) Case 1; (b) Case 2; (c) Case 3; and (d) Case 4.

produced by Ship_a could propagate to the body surface of Ship_b. But in Case 2, the near field flow around Ship_b could hardly be disturbed by the existence of Ship_a. Even though the positions of the ships in Cases 2 and 4 are the same, the wave patterns in these two cases are different. In Case 2, the diffracted and radiated waves are confined within a relatively smaller semi-wedge angle. But in Case 4, due to the smaller value of τ, the waves are expanded to cover a larger fan-shape region. These observations coincide with our theoretical assumption. Fig. 18 gives the diffracted and radiated wave profiles at port and starboard of Ship_b. It can be found that in Cases 1, 3 and 4, the wave elevation at port and starboard of the stern region of Ship_b is different. This explains why the sway, roll and yaw forces in these cases are very large. But in the fore region, the wave profiles tend to be identical to each other. It indicates that the waves produced by Ship_a could only propagate to the stern region of Ship_b in these cases. But in Case 2, the wave elevation at port and starboard of Ship_b is almost the same. Only a very small discrepancy can be observed in the stern area. It indicates that the quiescent region calculated by the present stationary phase method is not absolutely calm water. Due to the continuity of the pressure distribution on the free surface, the wave elevation could not suddenly drop to zero when the waves propagate across the critical line (the line corresponds to the semi-wedge angle, which is used to divide the wake and quiescent regions, as shown in Fig. 1). However, the wave elevation in the predicted quiescent region is not evident.

4. Hydrodynamic interaction diagram

It can be concluded from the numerical case study that the stationary phase method provides a general depiction of the wave propagation in the far-field. The critical line between the quiescent and wake region estimated from the far-field wave pattern can be generally adopted to estimate whether the hydrodynamic interaction is significant. However, the conclusion above is general and partial. The factors which determine the hydrodynamic interaction include several combinations of parameters: oscillation frequency, forward speed and transverse distance between two ships. Meanwhile the stationary phase method is not able to estimate accurately how much interactions are expected between two ships travelling in waves. Therefore, an accurate estimation of the critical line is desired, which requires numerous simulations varying Froude number, frequency and transverse distance. A similar approach which was adopted by Kashiwagi and Ohkusu (1991) to investigate the side-wall effects is introduced here to investigate ship-to-ship hydrodynamic interaction effects. In Kashiwagi and Ohkusu (1991) study, the side-wall effects are estimated by the difference between the hydrodynamic coefficients with side-wall and in the open sea. But in the present study, a more sophisticated parameter will be used to determine the hydrodynamic interaction effects. This parameter can be either A_{ij}^{ab} or A_{ij}^{aa}. As discussed above, the superscript '*ab*' directly reflect the interaction effect from the existence of the other ship. The coefficients with superscript '*ab*' are referred as the external-induced components while the superscript '*aa*' denotes the self-induced ones. For single ship case, the self-induced components do not exist.

Fig. 19 shows the external-induced components of the hydrodynamic coefficients, which is non-dimensionlized by the single ship results. Strictly speaking, there should be 36 independent components of each set of external-induced hydrodynamic coefficients if the two ships are not identical. Even in case of two identical ships, there are 21 independent components contained in the external-induced hydrodynamic coefficient matrix ($A_{ij}^{ab} = A_{ji}^{ab}$, $i=1,2,\ldots,6$; $j=1,2,\ldots,6$). In order to find the region where there is no hydrodynamic interaction, all of these components should be zero. In the numerical calculation, due to the numerical error,

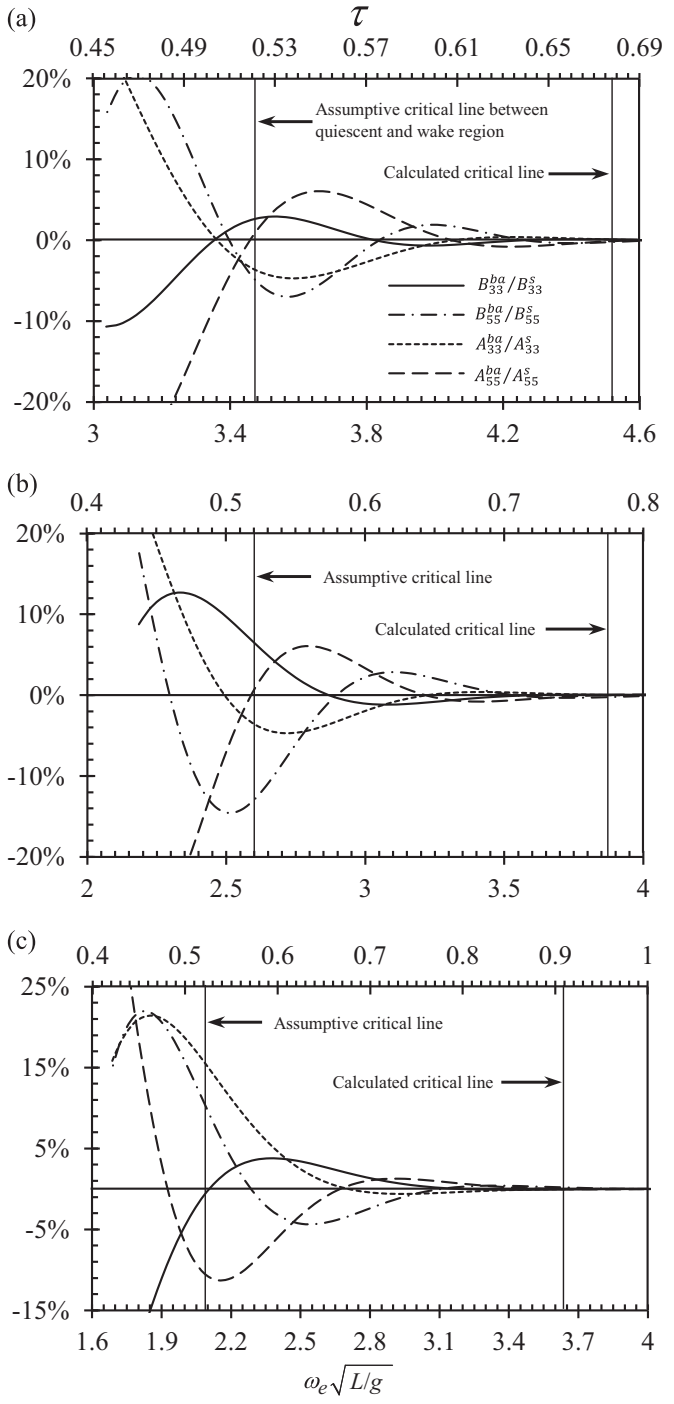

Fig. 19. External-induced hydrodynamic coefficients of identical Wigley hulls at $d/L=1$. (a) $F_n=0.15$; (b) $F_n=0.2$; (c) $F_n=0.25$. The results are non-dimensionlized by the corresponding values of single vessel in open sea, and the superscript 's' of A_{ij}^{s} or B_{ij}^{s} denotes the single vessel results.

these components are impossible to be zero, even for single vessel in open sea. Therefore, we have to set a permissible error. If the calculation values are bellow this permissible error, no hydrodynamic interaction is expected. In the present study, the permissible error is defined as 0.2%. Coincidently, the calculated results are quite consistent and convergent, even though the different components fluctuate with different amplitudes. Therefore, we only display four typical components in Fig. 19. From Fig. 5 we can find the assumptive critical $\tau=0.521$ estimated from the far-field asymptotic wave pattern at $d/L=1$. Theoretically, no

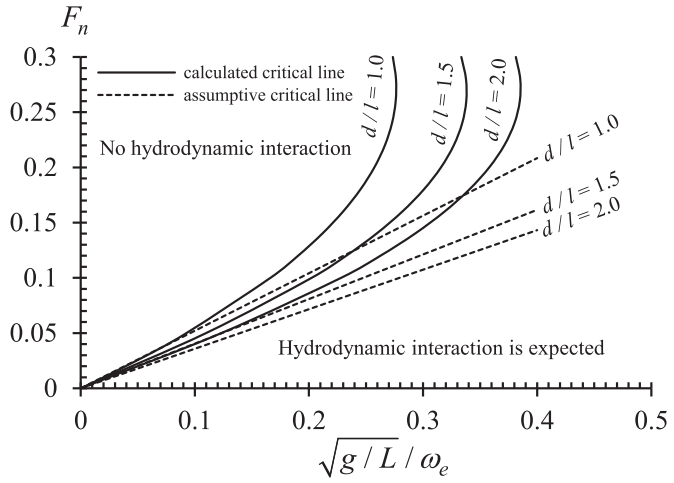

Fig. 20. Theoretical and numerical estimation of the critical lines showing whether the ship-to-ship hydrodynamic interaction effects are expected.

hydrodynamic interactions are expected at $\tau>0.521$. However, the numerical calculations presented in Fig. 19 shows a significant hydrodynamic interaction effect at $\tau=0.521$, and some components even experience an increasing trend at $\tau>0.521$. The hydrodynamic interaction effects gradually diminish and the external-induced hydrodynamic coefficients are convergent to the permissible error. At $F_n=0.15$, the curves are convergent to the permissible error at $\tau=0.677$. As the Froude number increases, the convergent point is extended to $\tau=0.773$ at $F_n=0.2$ and $\tau=0.909$ at $F_n=0.25$. It indicates as the Froude number increases, the actual quiescent region will shrink.

From Fig. 19 it can be found that for any given Froude number, we can always find a critical frequency. Therefore, we can determine the critical lines showing the existence of the hydrodynamic interaction effects as a function of Froude number, frequency and transverse distance. Results are shown in Fig. 20, where x-axis is the $\sqrt{g/L}/\omega_e=F_n/\tau$, y-axis is F_n. The ratio of y to x is parameter τ. In the present numerical calculation, as the two ships are in the same length ($\delta=1$), for a given value of d/L, the critical parameter τ is unique. Therefore, the dashed lines in Fig. 20 are linear and they represent the critical line estimated from the asymptotic far-field wave theory. The solid curves are the calculated critical lines, which approach the dotted lines at high frequency, where the wavelength is relatively small compared to the transverse distance between two ships and the theoretical estimation is valid. As the encounter frequency decreases, the discrepancies become evident and the range of hydrodynamic interaction effects expands. The difference between the dashed lines and solid curves is due to the effect of the near-field non-radiation local waves in the vicinity of the ships.

The permissible error can be various, for example, 1%. From Fig. 19 it can be found the critical parameter τ shifts to a smaller value and the discrepancies between the dashed lines and solid curves become small. However, the selection of the permissible error must be very careful. It should not be very large, for example 5%, otherwise the curves of the hydrodynamic coefficients will be subject to fluctuations before they tend to convergent. On the other hand, the results of different components will be inconsistent and individual diagrams are required.

5. Conclusions

In this paper, we presented a method based on Havelock form of the Green function to predict the far field wave pattern

produced by a translating and oscillating source. It was found that at $\tau > 0.25$, there existed a semi-wedge angle, which could be used to determine the critical line between the wake and quiescent region. This semi-wedge angle can be expanded to make a rapid estimation whether the hydrodynamic interaction between two ships advancing in waves is significant. It is assumed that if the two ships were located in each other's fan-shaped quiescent region, the hydrodynamic interactions could be minimized. Based on the semi-wedge angle, we established a formula to predict the minimum spacing between two ships.

In order to validate our theoretical estimation, a 3-D Ranking source panel method was developed to calculate the hydrodynamic properties of two Wigley hulls advancing in waves. Four typical case studies were designed. The comparisons provided an intuitional conclusion that the critical line estimated from far-field wave pattern can generally predict whether the hydrodynamic interaction is significant. But the theoretical expression cannot estimate accurately how much interactions are expected between two ships travelling in waves. Therefore, we performed a number of numerical calculations which cover a wide range of combinations of parameters including frequency, forward speed and transverse distance between two ships. Based on these calculations, we depicted a diagram showing whether the hydrodynamic interaction effects are expected. From the diagram, an evident discrepancy was observed between the theoretical estimation and numerical calculation, especially at the low frequency range. The theoretical estimation based on asymptotic far-field wave pattern under-estimated the range of hydrodynamic interaction effects. In practice, due to the near-field local waves, the hydrodynamic interaction exists in a wider range. The diagram depicted in Fig. 20 can be generally applied to estimate whether ship-to-ship hydrodynamic interaction effects are expected.

Acknowledgements

The work reported in this paper was performed within the project “Energy Efficient Safe Ship Operation (SHOPERA)” funded by the European Commission under contract No. 605221. The second author is also financially supported by National Natural Science Foundation of China under Grant no. NSFC51579122.

References

Battistin, D., 2000. Analytical, numerical and experimental investigation on the wave resistance interference phenomenon of trimaran configurations, In: Proceedings of the NAV2000 International Conference on Ship and Shipping Research, Venice, Italy.

Becker, E., 1958. Das Wellenbild einer unter der Oberfläche eines Stromes schwerer Flüssigkeit pulsierenden Quelle. J. Appl. Math. Mech. 38 (9–10), 391–399.

Chang, M.S., 1977. Computations of three-dimensional ship motions with forward speed, In: Proceedings of the 2nd International Conference on Numerical Ship Hydrodynamics, Berkeley, California.

Chen, G.R., Fang, M.C., 2001. Hydrodynamic interactions between two ships advancing in waves. Ocean Eng. 28, 1053–1078.

Chen, X.-B., Noblesse, F., 1998. Super Green Functions for Generic Dispersive Waves. IWWWFB13, Netherlands.

Das, S., Cheung, K.F., 2012. Scattered waves and motions of marine vessels advancing in a seaway. Wave Motion 49 (1), 181–197.

Day, A.H., Doctors, L.J., 2001. Rapid estimation of near- and far-field wave wake from ships and application to hull form design and optimization. J. Ship Res. 45 (1), 73–84.

Eggers, K., 1957. Uber das Wellenbild einer pilsieren den Storung in Translation, Schiff und Hafen, vol. 11, pp. 874–878.

Faltinsen, O.M., 2006. Hydrodynamics of High-Speed Marine Vehicles. Cambridge University Press, Cambridge.

Fang, M.C., Kim, C.H., 1986. Hydrodynamically coupled motions of two ships advancing in oblique waves. J. Ship Res. 30 (3), 159–171.

Hanaoka, T., 1953. On the velocity potential in Michell's system and the configuration of the wave-ridges due to a moving ship. J. Jpn. Soc. Nav. Arch. 93, 1–10.

Inglis, R.B., Price, W.G., 1982. A three-dimentional ship motion theory -the hydrodynamic coefficients with forward speed. Trans. R Inst. Nav. Arch. 124, 141–157.

Iwashita, H., 1997. Numerical seakeeping calculations based on the 3-D Green function method. Ship Technol. Res. 44, 111–132.

Kashiwagi, M., 1993a. Interaction forces between twin hulls of a catamaran advancing in waves (Part 1: Radiation problem). J. Jpn. Soc. Nav. Arch. 173, 119–131.

Kashiwagi, M., 1993b. Interaction forces between twin hulls of a catamaran advancing in waves (Part 2: Wave-exciting forces and motions in waves). J. Jpn. Soc. Nav. Arch. 174, 181–191.

Kashiwagi, M., Ohkusu, M., 1991. A new theory for side-wall interference effects on forward-speed radiation and diffraction forces. Ship Technol. Res. 38 (1), 17–48.

Kashiwagi, M., Endo, K., Yamaguchi, H., 2005. Wave drift forces and moments on two ships arranged side by side in waves. Ocean Eng. 32 (5–6), 529–555.

Kashiwagi, M., Ohkusu, M., 1989. Side-wall effects on hydrodynamic forces acting on a ship with forward and oscillatory Motions, In: Proceedings of the 5th International Conference on Numerical Ship Hydrodynamics, Hiroshima, Japan.

Kim, Y., Yue, D.K.P., Connell, B.S.H., 2005. Numerical dispersion and damping on steady waves with forward speed. Appl. Ocean Res. 27 (2), 107–125.

Li, L., 2001. Numerical Seakeeping Predictions of Shallow Water Effect on Two Ship Interactions in Waves (Ph.D. Thesis). Dalhousie University, Halifax.

Li, L., 2007. Numerical seakeeping simulation of model test condition for two-ship interaction in waves, In: Proceedings of the 26th International Conference on Offshore Mechanics and Arctic Engineering, San Diego, California, USA, p. OMAE2007-29328.

Lighthill, M.J., 1967. On waves generated in dispersive systems by travelling forcing effects, with applications to the dynamics of rotating fluids. J. Fluid Mech. 27 (4), 725–752.

Lighthill, M.J., 1978. Waves in Fluids. Cambridge University Press, Cambridge.

McTaggart, K., Cumming, D., Hsiung, C.C., Li, L., 2003. Seakeeping of two ships in close proximity. Ocean Eng. 30 (8), 1051–1063.

Miao, G.-P., Liu, Y.-Z., Yang, Q.-Z., Liu, Z.-Y., 1995. On the 3-D pulsating source of Michell type with forward speed. J. Hydrodyn. Ser. B 2, 84–95.

Newman, J.N., 1978. The theory of ship motion. Adv. Appl. Mech. 18, 221–283.

Noblesse, F., 2001. Analytical representation of ship waves. Ship Technol. Res. 48, 23–48.

Noblesse, F., Hendrix, D., 1992. On the theory of potential flow about a ship advancing in waves. J. Ship Res. 36 (1), 17–30.

Rahman, M., 1990. Three dimensional Green's function for ship motion in forward speed. Int. J. Math. Math. Sci. 13 (3), 579–590.

Ronæss, M., 2002. Wave Induced Motions of Two Ships Advancing on Parallel Course. NTNU, Trondheim.

Takagi, M., 1992. 3D Green function of oscillating body with forward speed on water of finite depth. Kansai Soc. Nav. Arch. J. 217, 67–76.

Tuck, E.O., Lazauskas, L., 1998. Optimum hull spacing of a family of multihulls. Ship Technol. Res. 45 (3), 180–195.

Wehausen, J.V., 1960. Surface Waves. Springer-Verlag, Berlin.

Wu, G.X., Eatock Taylor, R., 1987. A Green's function form for ship motions at forward speed. Int. Shipbuild. Prog. 34 (398), 189–196.

Wu, G.X., Eatock Taylor, R., 1989. The numerical solution of the motions of a ship advancing in waves, In: Proceedings of the 5th International Conference on Numerical Ship Hydrodynamics, Hiroshima, Japan.

Xu, Y., Dong, W.C., 2013. Numerical study on wave loads and motions of two ships advancing in waves by using three-dimensional translating-pulsating source. Acta Mech. Sin. 29 (4), 494–502.

Xu, Y., Dong, W.C., Xiao, W.B., 2013. Study on far field wave patterns and their characteristics of Havelock forn Green function. China Ocean Eng. 27 (3), 283–298.

Xu, X., Faltinsen, O.M., 2011. Time domain simulation of two interacting ships advancing parallel in waves, In: Proceedings of the 30th International Conference on Offshore Mechanics and Arctic Engineering, Rotterdam, The Netherlands, p. OMAE2011-49484.

Yang, C., Soto, O., Lohner, R., Noblesse, F., 2002. Hydrodynamic optimization of a trimaran. Ship Technol. Res. 49, 70–92.

Yuan, Z.M., He, S., Paula, K., Incecik, A., Turan, O., Boulougouris, E., 2015b. Ship-to-ship interaction during overtaking operation in shallow water. J. Ship Res. 59 (3), 172–187.

Yuan, Z.-M., Incecik, A., Day, A.H., 2014a. Verification of a new radiation condition for two ships advancing in waves. Appl. Ocean Res. 48, 186–201.

Yuan, Z.-M., Incecik, A., Jia, L., 2014b. A new radiation condition for ships travelling with very low forward speed. Ocean Eng. 88, 298–309.

Yuan, Z.-M., Incecik, A., Dai, S., Alexander, D., Ji, C.-Y., Zhang, X., 2015a. Hydrodynamic interactions between two ships travelling or stationary in shallow waters. Ocean Eng. 108, 620–635.